The Astrophysical Journal, 754:87 (22pp), 2012 August 1 doi:10.1088/0004-637X/754/2/87
© 2012. The American Astronomical Society. All rights reserved. Printed in the U.S.A.

DIFFERENT EVOLUTIONARY STAGES IN THE MASSIVE STAR-FORMING REGION W3 MAIN COMPLEX

Yuan Wang (王渊)[1,2,3], Henrik Beuther[2], Qizhou Zhang[4], Arjan Bik[2], Javier A. Rodón[5], Zhibo Jiang (江治波)[1], and Cassandra Fallscheer[6,7]

[1] Purple Mountain Observatory & Key Laboratory for Radio Astronomy, Chinese Academy of Sciences, Nanjing 210008, China; ywang@pmo.ac.cn
[2] Max-Plank-Institute for Astronomy, Königstuhl 17, Heidelberg 69117, Germany
[3] Graduate University of the Chinese Academy of Sciences, 19A Yuquan Road, Shijingshan District, Beijing 100049, China
[4] Harvard-Smithsonian Center for Astrophysics, 60 Garden Street, Cambridge, MA 02138, USA
[5] European Southern Observatory, Alonso de Córdova 3107, Vitacura, Casilla 19001, Santiago 19, Chile
[6] Department of Physics and Astronomy, University of Victoria, P.O. Box 355, STN CSC, Victoria, BC V8W 3P6, Canada
[7] National Research Council, 5071 West Saanich Rd., Victoria, BC V9E2E7, Canada
Received 2012 March 5; accepted 2012 May 23; published 2012 July 11

ABSTRACT

We observed three high-mass star-forming regions in the W3 high-mass star formation complex with the Submillimeter Array and IRAM 30 m telescope. These regions, i.e., W3 SMS1 (W3 IRS5), SMS2 (W3 IRS4) and SMS3, are in different evolutionary stages and are located within the same large-scale environment, which allows us to study rotation and outflows as well as chemical properties in an evolutionary sense. While we find multiple millimeter continuum sources toward all regions, these three subregions exhibit different dynamical and chemical properties, which indicate that they are in different evolutionary stages. Even within each subregion, massive cores of different ages are found, e.g., in SMS2, sub-sources from the most evolved ultracompact H II region to potential starless cores exist within 30,000 AU of each other. Outflows and rotational structures are found in SMS1 and SMS2. Evidence for interactions between the molecular cloud and the H II regions is found in the ^{13}CO channel maps, which may indicate triggered star formation.

Key words: ISM: individual objects (W3) – ISM: jets and outflows – ISM: molecules – stars: formation – stars: massive

Online-only material: color figures

1. INTRODUCTION

The formation and evolution of high-mass stars are still poorly understood. High-mass star formation not only proceeds exclusively in a clustered mode, but it becomes increasingly apparent that several episodes of high- and low-mass star formation can proceed sequentially within the same molecular cloud complex. Well-known examples are NGC 6334I and I(N) (e.g., Sandell 2000) or the S255 complex (e.g., Minier et al. 2005; Wang et al. 2011). Since the general molecular and stellar environment in these regions is almost the same within their different subregions, the environmental effects are minimized, which allows us to study the high-mass star formation in an evolutionary sense. Although there has been considerable progress in the general understanding of high-mass star formation over the last decade (e.g., Zinnecker & Yorke 2007; Beuther et al. 2007), many questions still remain open. The time evolution of the chemical and physical properties (e.g., rotating/infalling envelope, outflow) is still unclear.

Among the physical properties, massive molecular outflows are among the most studied phenomena. The outflows have been detected in various high-mass star formation stages, from the early stage as IRDCs to relatively evolved high-mass hot cores (e.g., Beuther et al. 2002; Wu et al. 2004; Zhang et al. 2005; Beuther & Nissen 2008; Fallscheer et al. 2009; Vasyunina et al. 2011). Observations toward the S255 complex show that outflows in the very young and cold region have low velocity and are relatively confined around the driving source, while the outflows associated with the relatively evolved high-mass protostellar objects exhibit large-scale collimated high-velocity structure (Wang et al. 2011). Beuther & Shepherd (2005) proposed an evolutionary sequence for the massive outflows in the high-mass protostellar phase: as the central object continues to accrete, it evolves from a B star to an O star and the outflows become less collimated under the pressure of the increased radiation and stellar wind.

Massive disks are a key component for high-mass stars to overcome radiation pressure and form through disk accretion (e.g., Krumholz et al. 2007, 2009; Kuiper et al. 2010). Rotating disks have been detected around intermediate-mass sources ($\sim$ 5–10 $M_\odot$; e.g., Zhang et al. 1998b; Cesaroni et al. 2005, 2007) but for higher mass objects, only rotating structures known as "toroids" (Cesaroni et al. 2007) have been detected (e.g., Beltrán et al. 2004; Beuther et al. 2005c; Fallscheer et al. 2009). These structures are not in Keplerian rotation and have typical radii of thousands of AU. Fallscheer (2010) sees an evolutionary trend where the size of the potential disk signature decreases from IRDCs to hot cores. Wang et al. (2011) also detected rotating toroids associated with high-mass protostellar objects and hot cores in the S255 complex, but the evolutionary trend is not clear according to their results.

From IRDCs to high-mass hot cores, massive star formation exhibits diverse chemical properties (e.g., Sutton et al. 1985; Schilke et al. 1997a, 2001; Beuther et al. 2009; Vasyunina et al. 2011; Wang et al. 2011), yet relatively few evolutionary details are known. High-resolution observations also show spatial variations among many species (e.g., Beuther et al. 2005b, 2009; Wang et al. 2011). Several theoretical studies exist on the chemical evolution during massive star formation (e.g., Charnley et al. 1997; Nomura & Millar 2004; Viti et al. 2004; Beuther et al. 2009); however, the high-resolution observational database to test these models is still relatively poor.

In this work, we present high-resolution Submillimeter Array (SMA) interferometry observations as well as single-dish CO(2–1) observations of three subregions (W3 SMS1, W3 SMS2, and W3 SMS3) within the same environment, W3 Main

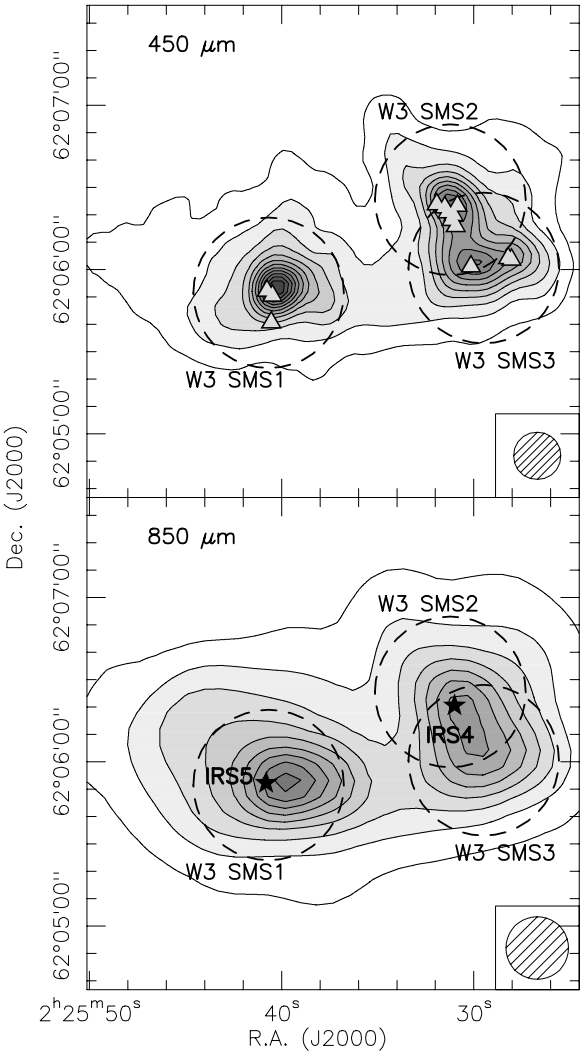

Figure 1. SCUBA 450 μm (top) and 850 μm (bottom) continuum images. The contour levels are in steps of 5σ starting at 5σ in both panels. For the 450 μm panel, $\sigma = 0.1$ Jy beam^{-1}, and for the 850 μm panel, $\sigma = 0.4$ Jy beam^{-1}. The dashed circles mark the primary beam of our SMA observations, the filled triangles in the top panel mark the SMA continuum sources we resolve, and the stars in the bottom panel mark the near-infrared sources.

(Ladd et al. 1993; Tieftrunk et al. 1998; Moore et al. 2007; Megeath et al. 2008). We study the evolution of the chemical and physical properties (outflows, rotation), ranging from potential starless cores to the most evolved ultracompact H II (UCH II) regions. W3 Main is part of the W3 molecular cloud and located at a distance of 1.95 ± 0.04 kpc (Xu et al. 2006). Single-dish submillimeter observations (Ladd et al. 1993) resolved three continuum sources, W3 SMS1, SMS2, and SMS3 (Figure 1).

The Eastern Region W3 SMS1. The central infrared source W3 IRS5 is associated with the hypercompact H II (HCH II) cluster W3 M (Claussen et al. 1994; Tieftrunk et al. 1997) with a total luminosity of $2 \times 10^5\ L_\odot$ (Campbell et al. 1995; Wynn-Williams et al. 1972), and coincides with water and OH masers (Claussen et al. 1994; Sarma et al. 2001, 2002; Imai et al. 2000; Gaume & Mutel 1987). The low radio luminosity of these HCH II regions suggests they might be stellar wind/jet sources (Hoare et al. 2007; Hoare & Franco 2007), and Wilson et al. (2003) found two of the HCH II regions show large proper motion and might be jet knots expelled from the massive stars in IRS5. In the high-resolution (<0.″1) radio observations done by van der Tak et al. (2005), these sources do not show elongated morphology and the authors argue that there are three HCH II regions together with several shock-ionized clumps. Megeath et al. (2005) reported seven near-IR sources with *Hubble Space Telescope* observations, and three of them have both mid-IR and radio continuum counterparts (van der Tak et al. 2005). Using the Plateau de Bure Interferometer, Rodón et al. (2008) resolved the main continuum source into five sources. Bipolar outflows and even multiple outflows are also reported (Claussen et al. 1984; Mitchell et al. 1992; Choi et al. 1993; Hasegawa et al. 1994; Imai et al. 2000; Rodón et al. 2008). It has been proposed that IRS5 is a proto-Trapezium and might emerge as a bound Trapezium similar to that in the Orion nebula (Megeath et al. 2005; Rodón et al. 2008). Megeath et al. (1996) identified an embedded cluster of 80–240 low-mass stars centered on IRS5, which in turn is surrounded by hundreds of low-mass stars (Feigelson & Townsley 2008). W3 IRS7 (associated with the UCH II region W3 F) and IRS3 (associated with the compact H II region W3 B) are also found here (Wynn-Williams et al. 1972; Harris & Wynn-Williams 1976; Tieftrunk et al. 1997).

The Northwestern Region W3 SMS2. The infrared source W3 IRS4 lies at the center of the continuum source with a luminosity of $6 \times 10^4\ L_\odot$ (Campbell et al. 1995). IRS4 is classified as an O8V–B0.5V star and is thought to be the exciting source of the UCH II region W3 C (Bik et al. 2011; Tieftrunk et al. 1997). The HCH II region W3 Ca lies east of IRS4 which indicates that a massive star is forming. OH masers and evidence for an outflow are also found toward IRS4 (Gaume & Mutel 1987; Hasegawa et al. 1994).

The Southwestern Region W3 SMS3. W3 SMS3, located south of W3 IRS4, is considered a quiescent region in W3 Main (Megeath et al. 2008). It exhibits strong millimeter continuum emission (Figure 1) but no other signs of active star formation such as near-infrared or mid-infrared emission (Ruch et al. 2007). Tieftrunk et al. (1998) found extended emission toward SMS3 with Very Large Array (VLA) NH_3 observations, which show quite narrow line widths toward this region. Tieftrunk et al. (1998) also found four compact NH_3 clumps with masses around 30 $M_\odot$ surrounding the main clump.

Furthermore, NIR imaging and spectroscopy studies by Bik et al. (2011) revealed an age spread of at least 2–3 Myr in W3 Main and suggested a sequential star formation process. While W3 SMS1 and SMS2 show signs of active star formation and are surrounded by an NIR cluster, SMS3 is still quiescent with no signs of ongoing star formation. Therefore, W3 Main is an ideal region to simultaneously investigate several sites of massive star formation at different evolutionary stages within the same over all environment.

2. OBSERVATIONS AND DATA REDUCTION

2.1. Submillimeter Array Observations

The W3 Main complex was observed in three fields with the SMA[8] on 2009 December 31 in the compact configuration and on 2010 January 30 in the extended configuration, both with seven antennas. The phase centers of the observations, which are known as W3-SMS1, W3-SMS2, and W3-SMS3, were R.A. $02^h25^m40.^s68$, decl. +62°05′51.″5 (J2000); R.A. $02^h25^m31.^s22$, decl. +62°06′25.″5 (J2000); and

[8] The Submillimeter Array is a joint project between the Smithsonian Astrophysical Observatory and the Academia Sinica Institute of Astronomy and Astrophysics and is funded by the Smithsonian Institution and the Academia Sinica.

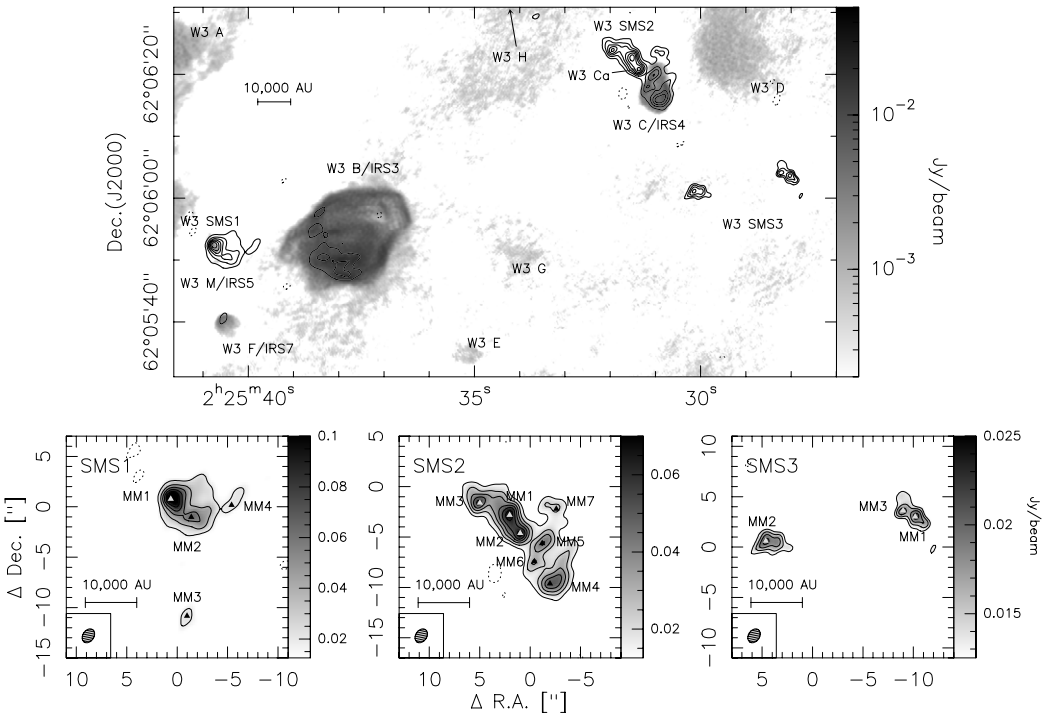

Figure 2. SMA 1.3 mm continuum maps of the W3 SMS1, SMS2, and SMS3 regions. Top panel: the VLA 22.5 GHz continuum image (Tieftrunk et al. 1997) overlaid with the SMA 1.3 mm continuum contours. The contour levels start at 5σ and are in steps of 5σ for SMS1 ($\sigma = 3.6$ mJy beam^{-1}), in steps of 4σ for SMS2 ($\sigma = 2.5$ mJy beam^{-1}), and in steps of 1σ in SMS3 region ($\sigma = 2.5$ mJy beam^{-1}). Bottom panels: the SMA 1.3 mm continuum maps of each region. The contour levels are the same as in the top panel. The dotted contours are negative features due to the missing flux with the same contour levels as the positive ones in each panel. Beams are shown at the bottom left of each panel. Filled triangles mark the millimeter sources detected.

R.A. $02^{h}25^{m}29\overset{s}{.}49$, decl. $+62°06'00\overset{''}{.}6$ (J2000), respectively. The SMA has two spectral sidebands, both 4 GHz wide and separated by 10 GHz. The receivers were tuned to 230.538 GHz in the upper sideband ($v_{\rm lsr} = -43$ km s^{-1}) with a spectral resolution of 1.2 km s^{-1}. For the compact configuration, the bandpass calibration was derived from the observations of the quasar 0854+201. Phase and amplitude were calibrated with regularly interleaved observations of the quasar 0136+478 ($15\overset{\circ}{.}8$ from the source). Since the flux measurements of the gain calibrator 0136+478 on 2009 December 31 are available in the SMA calibrator database, we do the flux calibration with this quasar, and the flux scale is estimated to be accurate within 20%. For the extended configuration, the bandpass calibration was derived from the quasar 3C273. Phase and amplitude were calibrated with regularly interleaved observations of the quasar 0102+584 (11° from the source). The flux calibration was derived from observations of Titan, and the flux scale is estimated to be accurate within 20%. We merged the two configuration data sets, applied different robust parameters for the continuum and line data, and obtained synthesized beam sizes between $1\overset{''}{.}5 \times 1\overset{''}{.}1$ (P.A. $-35°$) and $2\overset{''}{.}2 \times 1\overset{''}{.}8$ (P.A. $-34°$). The 3σ rms of the 1.3 mm (225 GHz) continuum image is ∼10.8 mJy beam^{-1} and the 3σ rms of the line data is 0.11 Jy beam^{-1} at 2 km s^{-1} spectral resolution. The flagging and calibration were done with the IDL superset MIR (Scoville et al. 1993) which was originally developed for the Owens Valley Radio Observatory and adapted for the SMA.[9] The imaging and data analysis were conducted in MIRIAD (Sault et al. 1995).

[9] The MIR cookbook by Chunhua Qi can be found at http://cfa-www.harvard.edu/~cqi/mircook.html

2.2. Short Spacing from the IRAM 30 m

To complement the CO(2–1) observations, which lack the short-spacing information, and to investigate the large-scale general outflow properties, we observed the three subregions with the HERA array at the IRAM 30 m telescope on 2011 February 21. The ^{12}CO(2–1) line at 230.538 GHz and the ^{13}CO(2–1) line at 220.399 GHz were observed in the on-the-fly mode. We mapped the whole region with a map of $4' \times 4'$ centered at R.A. $02^{h}25^{m}41\overset{s}{.}01$, decl. $+62°07'02\overset{''}{.}1$ (J2000). The sampling interval was $0\overset{''}{.}8$. The region was scanned once along the declination and right ascension directions, respectively, in order to reduce scanning effects. The spectra were calibrated with CLASS, which is part of the GILDAS software package. The ^{12}CO data have a beam size of 11″, and the rms noise level of the corrected $T_{\rm mb}$ scale is around 0.25 K at 1.2 km s^{-1} spectral resolution. The ^{13}CO data have the same beam size, but the rms noise is 0.35 K at 1.2 km s^{-1} spectral resolution.

After reducing the 30 m data separately, single-dish ^{12}CO and ^{13}CO data were converted to visibilities and then combined with the SMA data using the MIRIAD package task UVMODEL. The synthesized beam of the combined data is $3\overset{''}{.}0 \times 2\overset{''}{.}5$ (P.A. $-34°$).

3. RESULTS

3.1. Millimeter Continuum Emission

Figure 2 shows the 1.3 mm continuum maps of the three regions. We resolve several continuum sources in all three regions. Assuming optically thin dust emission, we estimate the gas mass and column density of the continuum sources following the equations outlined in Hildebrand (1983) and Beuther et al. (2005b). We assume a dust temperature of 40 K,

Table 1
Millimeter Continuum Peak Properties

Source	R.A. (J2000)	Decl. (J2000)	I_ν (mJy beam^{-1})	S_ν (mJy)	Mass ($M_\odot$)	N_{H_2} (10^{24} cm^{-2})	Free–Free I_ν / Measured I_ν	Free–Free S_ν / Measured S_ν
SMS1-MM1	02:25:40.77	+62:05:52.3	123	405	40	6.5	0.03	0.02
SMS1-MM2	02:25:40.48	+62:05:50.5	63	229	23	3.4	n/a	n/a
SMS1-MM3	02:25:40.54	+62:05:40.7	22	25	...	0.3	0.73	2.04
SMS1-MM4	02:25:39.91	+62:05:51.7	22	35	4	1.2	n/a	n/a
SMS2-MM1	02:25:31.51	+62:06:22.7	68	208	21	3.6	n/a	n/a
SMS2-MM2	02:25:31.36	+62:06:20.9	67	121	12	3.5	0.02	0.01
SMS2-MM3	02:25:31.93	+62:06:23.9	55	113	11	2.9	n/a	n/a
SMS2-MM4	02:25:30.94	+62:06:15.9	50	220	...	1.3	0.52	1.01
SMS2-MM5	02:25:31.05	+62:06:19.9	43	75	2	1.3	0.42	0.74
SMS2-MM6	02:25:31.16	+62:06:18.1	34	50	0.1	0.6	0.69	0.97
SMS2-MM7	02:25:30.85	+62:06:23.3	26	67	7	1.4	n/a	n/a
SMS3-MM1	02:25:28.04	+62:06:03.6	21	40	4	1.2	n/a	n/a
SMS3-MM2	02:25:30.15	+62:06:01.2	21	66	7	1.2	n/a	n/a
SMS3-MM3	02:25:28.21	+62:06:04.2	19	33	3	1.1	n/a	n/a

Notes. "n/a" indicates no free–free emission is detected toward this source. For sources SMS1-MM3 and SMS2-MM4, the free–free flux we obtain at 225 GHz is even larger than our SMA 1.3 mm measurements, so we do not have the mass estimation.

Table 2
SCUBA 850 μ m Continuum Data

Source	I_ν (Jy beam^{-1})	S_ν (Jy)	Mass ($M_\odot$)	N_{H_2} (10^{23} cm^{-2})
W3 SMS1	19	39	715	5.9
W3 SMS2	15	24	435	4.7
W3 SMS3	14	24	445	4.4

grain size of 0.1 μm, grain mass density of 3 g cm^{-3}, gas-to-dust ratio of 100, and a grain emissivity index of 2 (corresponding to $\kappa \approx 0.3$ cm^2 g^{-1} for comparison with Ossenkopf & Henning 1994). Here, we assume the same dust temperature for all the continuum sources to simplify the calculation. The fact that the continuum sources may have different temperatures (see Section 3.5) would also bring uncertainty to the mass results. The SMA continuum measurements listed in Table 1 are not corrected for the primary beam, since for SMS1 and SMS2, the primary beam correction would only change the flux of our detected continuum sources by $\leqslant$2%, and for SMS3 the flux would be changed by $\leqslant$10%. For the SMA continuum sources which are associated with radio emission, the free–free emission is subtracted. We assume optically thin free–free emission (spectral index $\sim$−0.1), and use the VLA 22.5 GHz flux (Tieftrunk et al. 1997) to estimate the free–free flux at 225 GHz. In the following, we label the millimeter sources according to a scheme consisting of the name of the large-scale region (SMS1 to SMS3) followed by the millimeter peaks within them, e.g., SMS1-MM1. The corrected results are shown in Table 1. For sources SMS1-MM3 and SMS2-MM4, the free–free flux we obtain at 225 GHz is even larger than our SMA 1.3 mm measurements, which is likely due to the fact that the VLA observations have better *uv* coverage and suffer less from missing flux than the SMA observations.

With the same setup, we also calculate the gas mass and the column density of the SCUBA 850 μm continuum peaks shown in Table 2 (the SCUBA data were downloaded from the archive; Di Francesco et al. 2008) and compare the results with the ones in Table 1. The masses we obtain from the SMA observations for the W3 SMS1, W3 SMS2, and W3 SMS3 are only 9%, 12%, and 3% of the SCUBA 850 μm measurements, respectively. For the

Table 3
Millimetric, Radio, NIR, and MIR Counterparts

MM	Radio[a]	NIR	MIR
SMS1-MM1	W3 M (a+b+c+d1+d2+f)	IRS5[b]	1+2[c]
SMS1-MM3	W3 F	IRS7[b]	...
SMS2-MM2	W3 Ca	IRS4-b[d]	IRS4-b[d]
SMS2-MM4	W3 C	...	...
SMS2-MM5	W3 C	IRS4-a[d]	...
SMS2-MM6	W3 C	...	...

Notes.
[a] Claussen et al. (1994); Tieftrunk et al. (1997).
[b] Wynn-Williams et al. (1972).
[c] van der Tak et al. (2005).
[d] Figures 3 and 8.

W3 SMS1 region, we resolve part of the H II region W3 B from the SMA observations (Figure 2). However, it is already near the edge of our SMA field of view, and the emission we recover should be dominated by free–free emission. Therefore, we do not include the emission at W3 B from the SMA observations for the comparison. Since our interferometer observations are not sensitive to spatial scales > 27″ (corresponding to the shortest baseline = 7.5 kλ), we filter out the smoothly distributed large-scale halo and observe only the compact cores. Furthermore, the observational fact that we filter out more flux for the youngest region W3 SMS3 indicates that at the earliest evolutionary stages the gas is more smoothly distributed than during later stages where the collapse produces more centrally condensed structures. Nevertheless, all of the column densities we derive are above the estimated threshold for high-mass star formation of 1 g cm^{-2} (Krumholz & McKee 2008), which corresponds to a column density of $N_{H_2} \sim 3 \times 10^{23}$ cm^{-2}.

W3 SMS1. The SMA continuum image of W3 SMS1 is shown in the bottom left panel of Figure 2. The SMA image reveals four continuum sources, SMS1-MM1, SMS1-MM2, SMS1-MM3, and SMS1-MM4 in this region. As shown in Table 3, the strongest source, SMS1-MM1, coincides with the near-infrared source W3 IRS5 and the HCH II region cluster W3 M (Claussen et al. 1994; Tieftrunk et al. 1997). It is also associated with the mid-infrared sources MIR1 and MIR2 detected by van der Tak

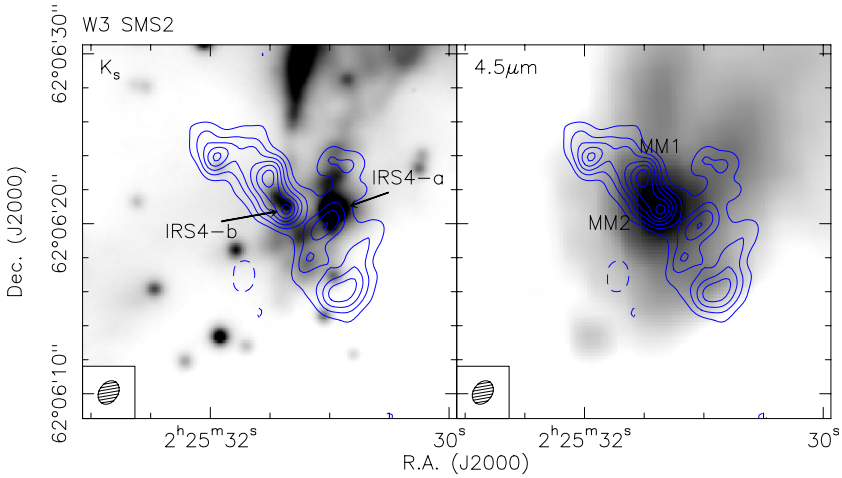

Figure 3. Left panel: the LBT-LUCI K_s-band image overlaid with the SMA 1.3 mm continuum map of the W3 SMS2 region. The K_s-band image is adapted from Bik et al. (2011). Right panel: the IRAC 4.5 μm short exposure time image (Ruch et al. 2007) overlaid with the SMA 1.3 mm continuum image. The IRAC post-bcd data were processed with pipeline version S18.7.0 and downloaded from the *Spitzer* archive. The contour levels are in steps of 4σ starting at 5σ ($\sigma = 2.5$ mJy beam^{-1}). The dashed contours are the negative features due to the missing flux with the same contour levels as the positive ones in each panel. The beam of the SMA map is shown at the bottom left corner.

(A color version of this figure is available in the online journal.)

et al. (2005). H_2O masers are also detected at the SMS1-MM1 position (Imai et al. 2000; Sarma et al. 2001, 2002). A previous higher resolution study shows that SMS1-MM1 is resolved into four individual 1.4 mm continuum sources (Rodón et al. 2008). SMS1-MM2 and MM4, which have not been detected before, are not associated with any infrared source. SMS1-MM4 is close to an NH_3 core detected by Tieftrunk et al. (1998). SMS1-MM3, south of SMS1-MM1, is associated with the infrared source W3 IRS7 and the UCH II region W3 F. Table 1 shows that the continuum emission at this region is dominated by free-free emission from the UCH II region and it is relatively evolved (Tieftrunk et al. 1997).

W3 SMS2. The bottom middle panel of Figure 2 presents the SMA continuum image of W3 SMS2. We detect seven continuum sources in this region. As listed in Table 3, SMS2-MM2 is associated with the HCH II region W3 Ca (Tieftrunk et al. 1997), and Figure 3 shows that SMS2-MM2 also coincides with another elongated infrared source, IRS4-b, which could be tracing the jet driven by SMS2-MM2 (see Figure 13 in Section 3.3). The elongated infrared source IRS4-b is very luminous in *Spitzer*/IRAC bands and dominates the mid-infrared emission here. The NIR source IRS4 marked here as IRS4-a fades out (Figure 3; Ruch et al. 2007). The top panel of Figure 2 shows that SMS2-MM4, SMS2-MM5, and SMS2-MM6 are associated with the ultracompact drop-shaped H II region W3 C, and Table 1 shows that the continuum emission of these three sources is dominated by the free–free emission from the UCH II region W3 C. This indicates that SMS2-MM4, SMS2-MM5, and SMS2-MM6 are just part of the UCH II region W3 C. The other three continuum sources, SMS2-MM1, MM3, and MM7, are not associated with any infrared or radio continuum source. They are likely to be at a very young evolutionary stage.

W3 SMS3. The SMA continuum image of W3 SMS3 is shown in the bottom right panel in Figure 2. The SMA observations resolve three continuum peaks in this region. These continuum sources are not associated with any near-infrared or radio source. The *Spitzer*/MIPS 24 μm map also shows no emission toward this region (Ruch et al. 2007). Meanwhile, the gas mass is only 3% of the SCUBA 850 μm measurements, which indicates that the gas in this region is smoothly distributed, indicative of an early evolutionary stage. All these features indicate that W3 SMS3 is an extremely young region.

3.2. Spectral Line Emission

We detect 41 lines from 13 species toward all three regions. In addition to the three CO isotopologues ^{12}CO, ^{13}CO, and $C^{18}O$, we also detect dense/hot gas tracers CH_3CN, CH_3OH, HNCO, HC_3N, OCS, shock tracer SiO, temperature determinator H_2CO, ionized gas tracer hydrogen recombination line H30α, and many SO and SO_2 isotopologues. The detailed chemical properties of each region will be explained in the following sections. We extract spectra of several molecular transitions at the position of each continuum peak within one beam size (2″.1 × 1″.7 for the lower sideband and 2″.0 × 1″.6 for the upper sideband), and the detected lines are listed in Table 6. Figure 4 shows the spectra toward SMS1-MM1 and SMS3-MM1 as examples.

W3 SMS1. In the W3 SMS1 region, we detect 36 lines from 12 species. Besides the three CO isotopologues, we also detect many sulfur-bearing species (^{13}CS, OCS, SO, SO_2, and their isotopologues), some dense gas molecules which are usually used to trace high-mass hot cores, such as CH_3OH, CH_3CN (Nomura & Millar 2004; Beuther et al. 2009; Sutton et al. 1985), and the well-known kinetic temperature determinator H_2CO (Mangum & Wootten 1993; Jansen et al. 1994; Mühle et al. 2007; Watanabe & Mitchell 2008). All the lines we detect have lower energy levels $E_{\rm lower}/k$ between 5.3 and 881 K (Table 6).

Figures 5 and 6 present the integrated line maps of all species (except SiO, ^{12}CO, and ^{13}CO which will be discussed in detail in Section 3.3). For $CH_3CN(12_k–11_k)$, we only present the line map of $k = 0, 1$, since the other line maps are similar to the one shown. For CH_3OH, we only present the line maps of two transitions, and for H_2CO we only show the map for one transition. The $CH_3OH(10_{2,8}–9_{3,7})$A+ line map shows an elongated structure closely aligned with the direction of outflow-a (see Figure 11, Section 3.3). All the other CH_3OH and CH_3CN lines do not peak exactly on any continuum source but somewhere between SMS1-MM1 and SMS1-MM2 (Figure 5). We derive the peak positions of the $CH_3CN(k = 0, 1)$, $CH_3OH(4_{2,2}–3_{1,2})$E, and H30α integrated emission through Gaussian fitting, and list the results in Table 4.

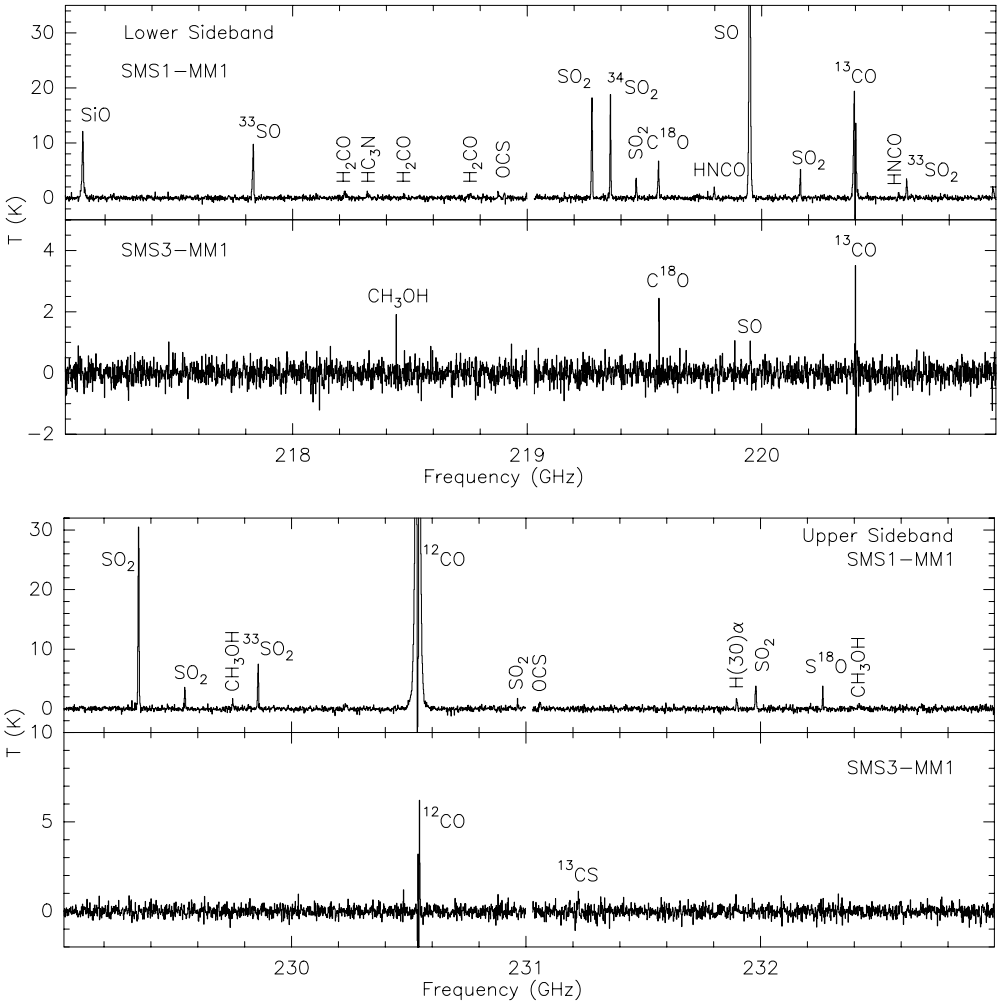

Figure 4. Upper and lower sideband spectra extracted toward SMS1-MM1 and SMS3-MM1 with a resolution of 2 km s^{-1} per channel. The SO line and the ^{12}CO line in SMS1-MM1 are not fully plotted, which go to 84 K and 94 K, respectively. The small gap in each spectrum is an effect of the data reduction process, since each sideband is divided into two parts to be processed separately.

All three H_2CO lines show an elongated structure which extends in the northwest–southeast direction centered between the SMA continuum peaks SMS1-MM1 and SMS1-MM2. ^{13}CS line emission is offset from the SMA continuum peaks (Figure 5); similar offset $C^{34}S$ emission has also been found by Beuther et al. (2009). The hydrogen recombination line H30α is also detected toward SMS1-MM1, SMS1-MM3, and the H II region W3 B. Table 4 shows that the H30α peak at SMS1-MM1 is between the compact radio sources a and b (Claussen et al. 1994; Tieftrunk et al. 1997), and the emission might be the joint contribution of sources a, b, c, d1/d2, and f (Claussen et al. 1994; Tieftrunk et al. 1997). We detect many sulfur-bearing lines in this region. Figure 6 shows that all lines of SO and SO_2 isotopologues peak on the continuum source SMS1-MM1. Furthermore, the SO(6_5–6_4) line emission shows an elongated structure along the redshifted outflow (outflow-b in Figure 11; see Section 3.3) and could be affected by the outflow.

Most of the lines we detected in the SMS1 region are found toward SMS1-MM1, except the *k*-ladder lines of CH_3CN and the ^{13}CS lines. Far fewer lines are detected toward SMS1-MM2. Although the hot core tracers CH_3CN and CH_3OH are detected toward SMS1-MM2, the line emission peaks do not coincide with the continuum peak of SMS1-MM2. In addition, CH_3OH emission is also associated with the redshifted outflow of SMS1-MM1 (outflow-a in Figure 11; see Section 3.3), these lines are more likely due to the shock heating excited by the outflow. As a typical dense gas molecule, we cannot explain why no CH_3CN emission is detected toward SMS1-MM1. Many lines we label as detected toward SMS1-MM2 in Table 6 do not show an emission peak at SMS1-MM2 (Figures 5 and 6). The reason could be that some of the lines associated with SMS1-MM1 are actually extended emission and not confined to SMS1-MM1. Since we extract the spectra with one beam size, the spectra we extract toward SMS1-MM2 could be affected by the extended emission around SMS1-MM1, which means the actual number of lines which originate from SMS1-MM2 is even smaller. For SMS1-MM4, only the three CO lines, the SO(6_5–5_4) line, and the SiO line are detected (Figure 11, see Section 3.3). SiO is a well-known shock tracer (e.g., Schilke et al. 1997b), and the SiO emission detected from SMS1-MM4 is clearly due to the shock excited by the outflow. Therefore, SMS1-MM2 and SMS1-MM4 appear to be chemically younger than SMS1-MM1. No lines are detected toward SMS1-MM3 except CO and H30α lines which indicates that this source is relatively evolved and has no high density gas in its circumstellar environment.

W3 SMS2. Here, we detect 27 molecular lines from 11 species (^{12}CO, DCN, H_2CO, HC_3N, CH_3OH, OCS, HNCO, SO, SO_2, ^{13}CS, CH_3CN) and two additional CO isotopologues (^{13}CO and

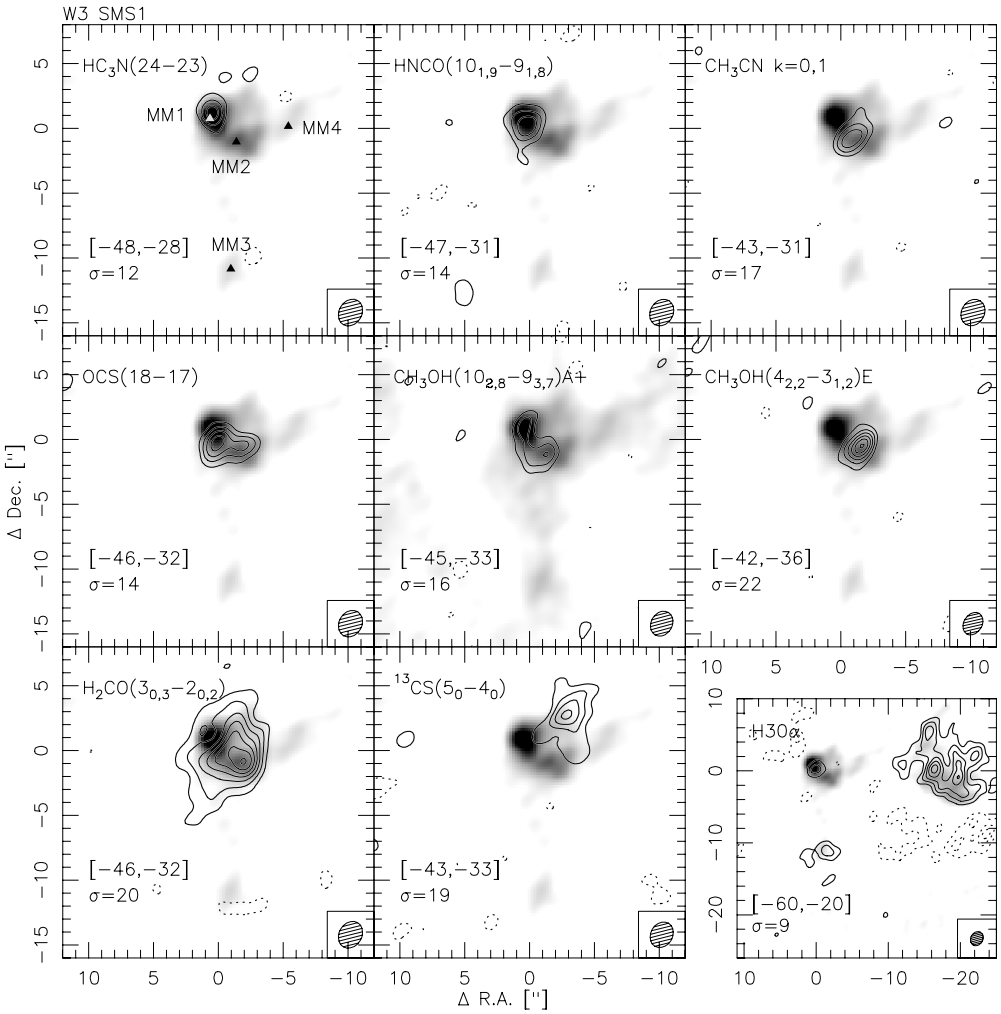

Figure 5. W3 SMS1 molecular line integrated intensity maps overlaid on the SMA 1.3 mm continuum emission in the background. Contour levels start at 3σ and continue in steps of 2σ. The σ value for each transition is shown in the respective map in mJy beam^{-1}. The dotted contours are the negative features due to the missing flux with the same contour levels as the positive ones in each panel. The integrated velocity ranges are shown in the bottom left part of each panel in km s^{-1}. The synthesized beams of the molecular line integrated intensity images are shown in the bottom right of each panel. The (0, 0) point in each panel is R.A. $02^{h}25^{m}40\overset{s}{.}68$, decl. $+62^{\circ}05'51\overset{''}{.}5$ (J2000).

$C^{18}O$) with lower energy levels $E_{\rm lower}/k$ between 5.3 K and 315 K (Table 6). The hydrogen recombination line H30α is also detected toward SMS2-MM4, MM5 and MM6. Figure 7 shows the integrated line maps of all species (except the CO isotopologues, which will be discussed in Section 3.3).

Figure 7 shows that the hot and dense gas tracers, such as CH_3CN and CH_3OH, all peak on the SMA continuum source SMS2-MM2, which indicates the massive hot core nature of this continuum source. The H_2CO line also peaks at SMS2-MM2 and exhibits extended emission toward SMS2-MM1, MM3, and MM7. Other detected lines at SMS2 all peak at SMS2-MM2 except for DCN and ^{13}CS. The DCN line shows extended emission toward SMS2-MM1, MM3, and MM7, and the ^{13}CS line peaks at SMS2-MM3 and extends toward SMS2-MM1. All these features show that the continuum sources SMS2-MM1, MM3, and MM7 are at a younger evolutionary stage than SMS2-MM2. The detection of the H30α line emission toward SMS2-MM4, MM5, and MM6 shows again that these three continuum sources are part of the UCH II region W3 C.

The HC_3N and H_2CO integrated intensity maps show an extra peak to the north of the SMA continuum source SMS2-MM1 (Figure 7), and one IRAC 8 μm point source is found there (Figure 8). We name this 8 μm point source as IRS4-c, which is not visible at shorter wavelengths and does not have a millimeter continuum counterpart. These features show the peculiar properties of IRS4-c.

W3 SMS3. Far fewer lines were observed in the W3 SMS3 region. We detect seven lines from five species (^{12}CO, DCN, CH_3OH, SO, and ^{13}CS) and two additional CO isotopologues (^{13}CO and $C^{18}O$) with lower energy levels $E_{\rm lower}$ between 5.3 K and 35 K (Table 6). Compared to the other two regions, the excitation temperatures of the lines we detect in this region are much lower, which indicates that W3 SMS3 has a much lower temperature than the other two. Figure 9 shows the integrated line images of all species (except the three CO isotopologues which will be discussed in Section 3.3). The DCN line emission peaks at SMS3-MM2 and the ^{13}CS line peaks at SMS3-MM1 and MM2. The CH_3OH and SO also peak toward the region between SMS3-MM1 and SMS3-MM2 and exhibit extended emission in the direction of one of the continuum sources. Because the continuum emission is usually more compact than most molecular emission from SO or CH_3OH, missing flux is unlikely to explain the discrepancy. The extended gas emission in regions without detected continuum rather indicates a peculiar

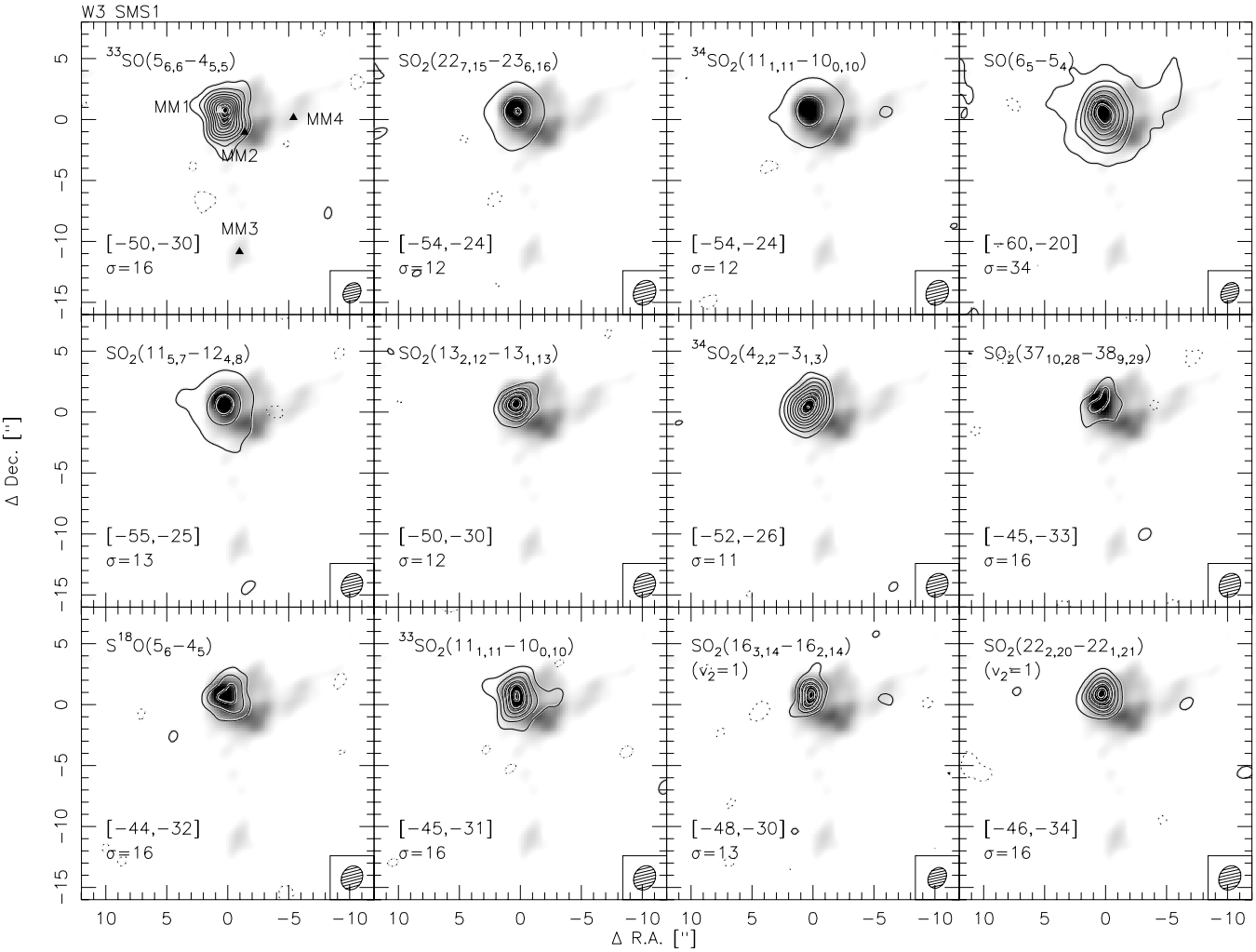

Figure 6. W3 SMS1 sulfur-oxide line integrated intensity map overlaid on the SMA 1.3 mm continuum emission in the background. Contour levels start at 3σ and continue in steps of 3σ, except for the SO(6_5–5_4) panel, in which the contour step is 10σ. The σ value for each transition is shown in the respective map in mJy beam^{-1}. The dotted contours are the negative features due to the missing flux with the same contour levels as the positive ones in each panel. The integrated velocity ranges are shown in the bottom left part of each panel in km s^{-1}. The synthesized beams of the molecular line integrated intensity images are shown in the bottom right of each panel. The (0, 0) point in each panel is R.A. 02^{h}25^{m}40^s.68, decl. +62°05′51″.5 (J2000).

chemistry. The small number of lines detected in SMS3 indicates that SMS3 is chemically younger than SMS1 and SMS2.

3.3. The Molecular Outflows

Figure 10 shows the ^{12}CO channel map of the single-dish data only. The $v_{\rm lsr}$ of SMS1, SMS2, and SMS3 are −39.3 km s^{-1}, −42.8 km s^{-1}, and −42.8 km s^{-1}, respectively. A redshifted outflow component which extends toward the southwest is found associated with SMS1. However, the blueshifted component is relatively confined around the continuum peak. We believe this outflow is in the northeast–southwest (NE–SW) direction. In the SMS2 region, one blueshifted emission structure toward the northwest and northeast, which is associated with the SMA continuum source SMS2-MM2, was detected (from panel −52.8 km s^{-1} to −45.6 km s^{-1} in Figure 10). However, the single-dish channel map does not show much redshifted emission in this region. Similarly in the SMS3 region, the single-dish channel map does not show much high-velocity emission. We combine the SMA data and 30 m data to study the outflow properties.

W3 SMS1. The top panels in Figure 11, from left to right, show the ^{12}CO(2–1) outflow image of the W3 SMS1 region derived from the SMA data only, combined SMA+30 m data, and the IRAM 30 m data only. The bottom panel in Figure 11 shows the SiO(5−4) outflow map observed with SMA. Imai et al. (2000) and Rodón et al. (2008) observed multiple outflows which are associated with W3 IRS5, and Figure 11 also shows the complicated outflow environment. By comparing our outflow data with previous work which has been done for this region (Claussen et al. 1984; Mitchell et al. 1991; Choi et al. 1993; Hasegawa et al. 1994; Imai et al. 2000; Gibb et al. 2007; Rodón et al. 2008), we identify four outflows in this region and mark them with four lines in the SMA+30 m panel of Figure 11. Figure 12 shows the position–velocity (PV) diagrams of the ^{12}CO SMA+30 m outflow observations.

Outflow-a. The NE–SW outflow shown in Figure 10 is denoted as outflow-a, which is also seen in all the ^{12}CO outflow panels of Figure 11. The blueshifted part of outflow-a is not as prominent as the redshifted part. This outflow and its asymmetric structure have also been detected by Claussen et al. (1984), Mitchell et al. (1991), Choi et al. (1993), and Hasegawa et al. (1994). Since the CO outflow emission traces the entrained gas (Arce et al. 2007), it can be significantly affected by the environment. Therefore, the asymmetric structure of outflow-a could be due to different properties of the ambient gas. Outflow

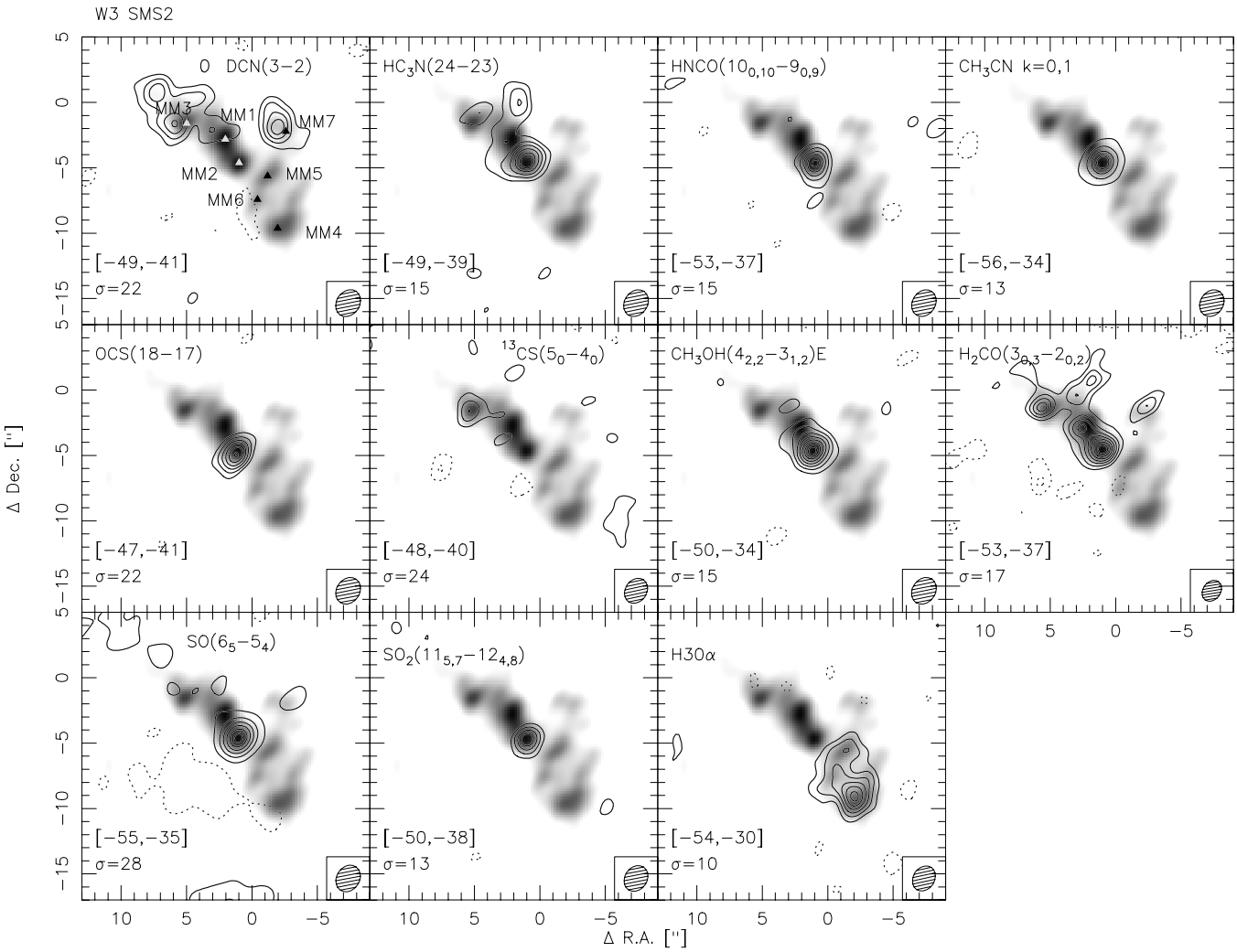

Figure 7. W3 SMS2 molecular line integrated intensity images overlaid on the SMA 1.3 mm continuum emission in the background. Contour levels start at 3σ and continue in steps of 2σ except for the CH_3CN and $SO(6_5–5_4)$ panels, in which the contour step is 5σ/level and 10σ/level, respectively. The σ value for each transition is shown in the respective map in mJy beam^{-1}. The dotted contours are the negative features due to the missing flux with the same contour levels as the positive ones in each panel. The integrated velocity ranges are shown in the bottom left part of each panel in km s^{-1}. The synthesized beams of the molecular line integrated intensity images are shown in the bottom right of each panel. The (0, 0) point in each panel is R.A. $02^h25^m31^s.22$, decl. $+62°06'25''.52$ (J2000).

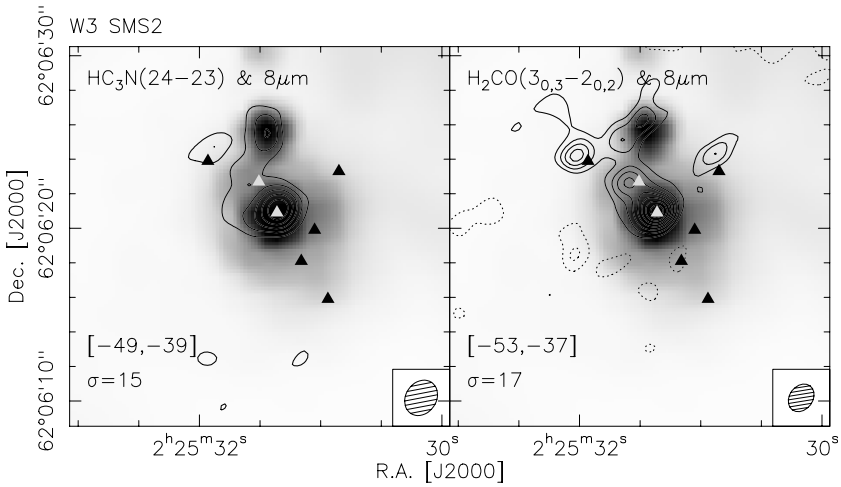

Figure 8. IRAC 8 μm short exposure time image (Ruch et al. 2007) overlaid with the SMA HC_3N (left) and H_2CO (right) integrated intensity images. The filled triangles mark the SMA millimeter sources we detect. The IRAC post-bcd data were processed with pipeline version S18.7.0 and downloaded from the *Spitzer* archive. Contour levels start at 3σ and continue in steps of 2σ. The σ value for each transition is shown in the respective map in mJy beam^{-1}. The dotted contours are the negative features due to the missing flux with the same contour levels as the positive ones in each panel. The synthesized beams of the molecular line integrated intensity images are shown in the bottom right of each panel.

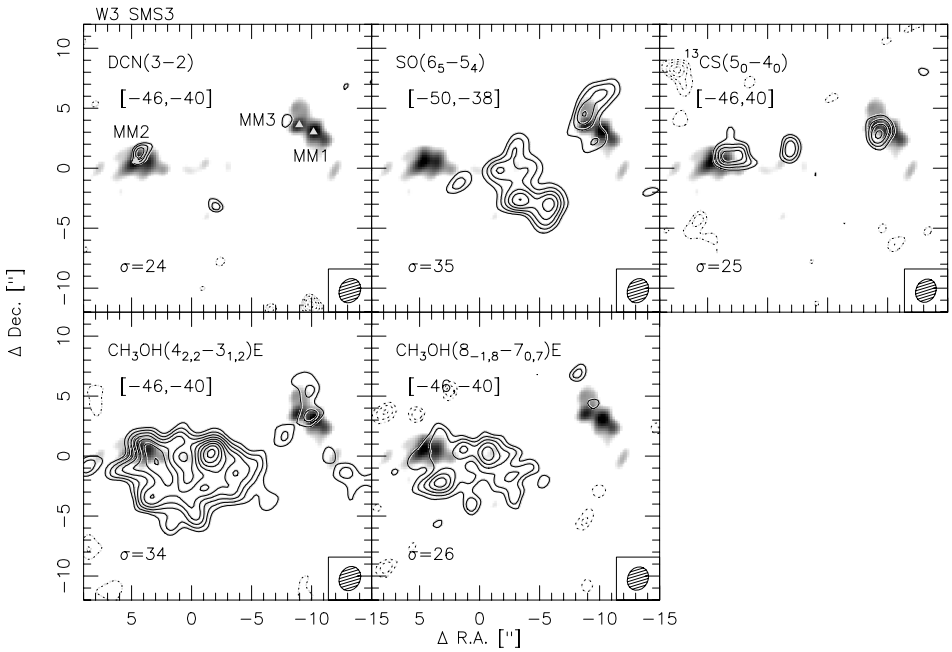

Figure 9. W3 SMS3 molecular line integrated intensity images overlaid on the SMA 1.3 mm continuum emission. Contour levels start at 3σ and continue in steps of 1σ except for the DCN(3–2) panel, in which the contour step is 0.5σ per level. The σ value for each transition is shown in the respective map in mJy beam^{-1}. The dotted contours are the negative features due to the missing flux with the same contour levels as the positive ones in each panel. The integrated velocity ranges are shown in the bottom left part of each panel in km s^{-1}. The synthesized beams of the molecular line integrated intensity images are shown in the bottom right of each panel. The (0, 0) point in each panel is R.A. $02^{h}25^{m}29^{s}.49$, decl. $+62°06'00''.6$ (J2000).

"Flow A," identified with H_2O maser observations by Imai et al. (2000), is in a similar direction as outflow-a. We believe that the outflow "Flow A" and our outflow-a actually trace different parts of the same outflow. Outflow "Flow A" traces the inner small-scale structure and outflow-a traces the outer large-scale structure. The different directions between these two outflows could be due to precession of this outflow caused by the relative motions of the driving source of outflow "Flow A" with respect to that of "Flow B" found by Imai et al. (2000). However, this outflow does not show up in our SiO observations or the SiO observations of Rodón et al. (2008). The emission of these two molecules does not necessarily stem from exactly the same environment because unlike CO outflow emission, SiO emission traces strong shocks in dense molecular gas (Schilke et al. 1997b). The other three outflows can only be detected in the SMA and SMA+30 m panel. The PV diagram of outflow-a (panel (a), Figure 12) shows that the far end of the redshifted part resembles the outflow Hubble law with increasing velocity at a larger distance from the outflow center (e.g., Arce et al. 2007).

Outflow-b. Outflow-b is more or less in the east–west (E–W) direction, and is also shown in the SiO outflow map. The PV diagram (panel (b), Figure 12) shows a weak Hubble-law profile (Arce et al. 2007). This outflow was first detected by SiO emission (Gibb et al. 2007) and is only detected in the better resolution SMA and SMA+30 m maps. Rodón et al. (2008) claimed that one of their SiO outflows (their SiO-c) could represent the SiO outflow detected by Gibb et al. (2007) (i.e., our outflow-b). However, the outflow detected by Rodón et al. (2008) has the redshifted part in the east and the blueshifted part in the west, which is exactly the opposite of our outflow-b. Thus, we believe this SiO outflow traces a different outflow than the one in Rodón et al. (2008).

Outflow-c. All the PV diagrams (Figure 12) are dominated by one strong outflow, which is aligned very close to the line of sight at or near the zero-offset point. Rodón et al. (2008) also reported an outflow that is aligned very close to the line of sight. Along line c in Figure 11, the SiO outflow map shows an opposite red–blue direction compared to the CO outflow map in the vicinity of SMS1-MM1. Thus, we suggest that there is another outflow, outflow-c, which is aligned close to the line of sight. Line c in Figure 11 does not represent the direction of outflow-c, we just choose it to produce the PV diagram (panel (c) in Figure 12), which shows a symmetric velocity profile. This outflow is also detected in the SiO outflow map (Figure 11). Rodón et al. (2008) identified two SiO outflows which are aligned close to the line of sight, and outflow-c is likely the joint contribution of these two SiO outflows. Figure 6 shows that the emission from all the SO_2 and its isotopologues peaks on the SMA continuum source SMS1-MM1. Since SO_2 is known to be enriched by shock interactions with outflows (Beuther et al. 2009), the strong SO_2 emission at all different energy levels could be due to the shock driven by outflow-c.

Outflow-d. Outflow-d is roughly in the north–south direction, and is also shown in the SiO outflow map. This N–S outflow matches the water maser outflow found by Imai et al. (2000) and one of the outflows detected from proper motions of compact radio sources by Wilson et al. (2003).

The bottom panel of Figure 11 shows that the central part of the blueshifted SiO outflow emission is offset to the SW direction by $\sim 2''$ from the continuum peak of SMS1-MM1. This offset could be produced by the outflow SiO-c identified by Rodón et al. (2008; the redshifted part is in the E direction and the blueshifted part is in the W direction). Two additional outflows identified by Rodón et al. (2008; their SiO-d and SiO-e) are not found in our observations. In principle, we cannot exclude that this outflow is just a wide-angle outflow, however, from our point of view the diverse data and the observations mentioned above rather favor a multiple outflow scenario.

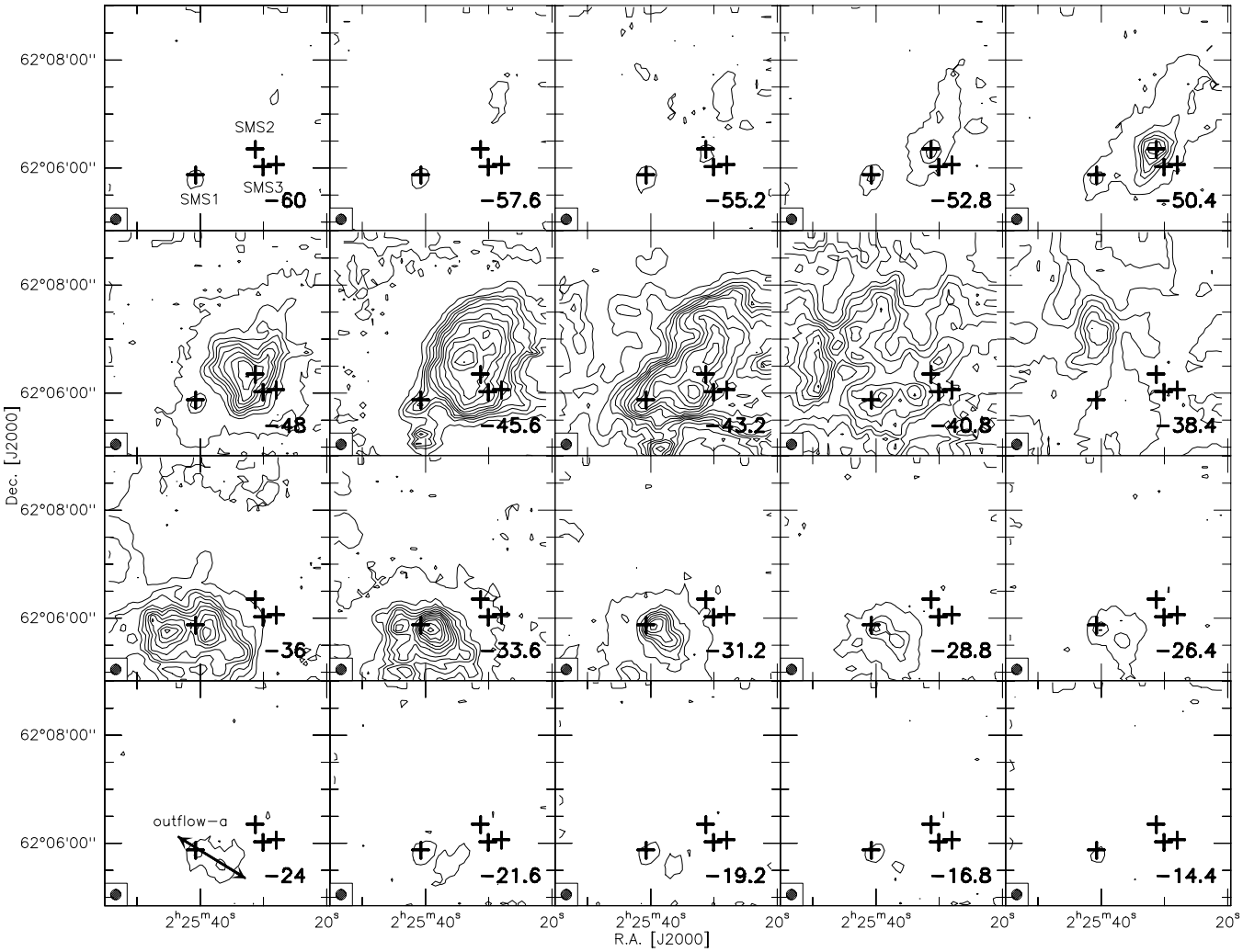

Figure 10. Single-dish ^{12}CO channel map with a spectral resolution of 2.4 km s^{-1}. The contour levels start at 5σ and continue in steps of 30σ (1σ = 0.2 K). The crosses mark the positions of the SMA continuum sources SMS1-MM1, SMS2-MM2, SMS3-MM1, and SMS3-MM2. The arrow in the bottom left panel marks the outflow-a we identify. The $v_{\rm lsr}$ of SMS1, SMS2, and SMS3 are −39.3 km s^{-1}, −42.8 km s^{-1}, and −42.8 km s^{-1}. The beam of the single-dish data is shown in the bottom left corner of each panel.

The outflow map of SMS1 shows that the driving source of all the outflows we found here is the SMA continuum source SMS1-MM1, which was resolved into four 1.4 mm continuum sources by Rodón et al. (2008). They claim the driving source of their outflow SiO-e may be the NH_3 feature close to the projected center of SiO-e. This NH_3 feature is associated with our SMA continuum source SMS1-MM4, and we do not see an outflow driven by this source. The existence of multiple outflows driven by SMS1-MM1 also confirms that SMS1-MM1 is a proto-Trapezium system as proposed by Megeath et al. (2005).

W3 SMS2. The top panels in Figure 13 show the W3 SMS2 ^{12}CO(2–1) outflow maps. The SMA and SMA+30 m panels show that the blueshifted outflow emission is strong and extended. Although the redshifted outflow emission is relatively weak and confined to the SMA continuum source SMS2-MM2 region, it still has a peak intensity of 16σ (1σ = 30 mJy beam^{-1}) in the SMA outflow map. In the 30 m only outflow map, the redshifted outflow emission is smoothed out and only the strong blueshifted emission remains.

The bottom panel in Figure 13 shows the SO(6_5–5_4) outflow map observed with the SMA. The redshifted SO emission coincides with the blueshifted component SO-a and only peaks on SMS2-MM2, the same as the ^{12}CO(2–1) redshifted emission. The blueshifted SO emission shows two lobes: one lobe peaks on the continuum source SMS2-MM2 that we denote as SO-a, and the other one extends toward the northeast direction that we denote as SO-b. There is also blueshifted ^{12}CO emission in the SO-b direction, but it is not as clear as SO-b. Since the UCH II region W3 C is next to SMS2-MM2, the ambient molecular gas of SMS2-MM2 could easily be blown away and affect the outflow by making the redshifted and blueshifted outflow components asymmetric. We believe that SMS2-MM2 is the driving source of this outflow and the outflow is in the northeast-southwest direction. However, we cannot rule out the possibility of multiple outflows.

The left panel of Figure 14 shows the PV diagrams of the combined SMA+30 m ^{12}CO(2–1) observations. The PV plot cuts follow the straight lines shown in Figure 13, top middle panel. The diagram is dominated by strong blueshifted emission, and the redshifted emission is quite weak. The right panel of Figure 14 shows the PV diagram of the SMA SO(6_5–5_4) observations. The PV plot cuts follow the straight lines shown in Figure 13, bottom panel. The diagram shows that a pair of blueshifted and redshifted emission features remains close to the center of the outflow (i.e., the SMS2-MM2 peak position)

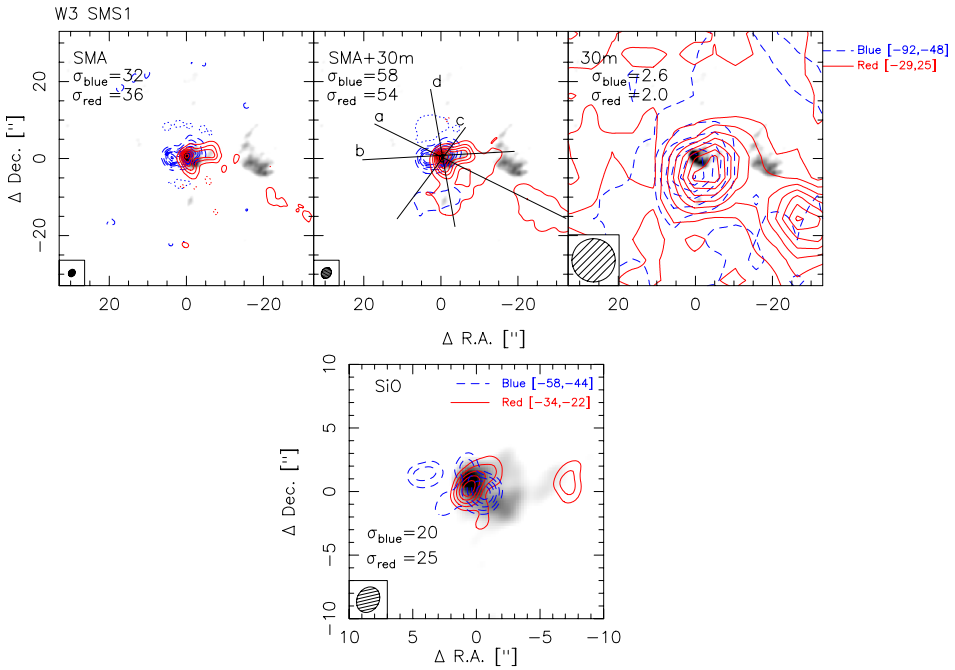

Figure 11. W3 SMS1 outflow maps observed with the SMA and IRAM 30 m telescope. The gray scale in all panels is the SMA 1.3 mm continuum image. Top panels: the full and dashed contours show the redshifted and blueshifted ^{12}CO(2–1) outflow emission, respectively. The top left panel presents the SMA data only map, the middle one is the combined SMA+30 m data, and the right one is the IRAM 30 m data only map. The velocity-integration ranges are shown in the top right. All the CO emission contour levels start at 4σ and continue in steps of 8σ. The four solid lines in the SMA+30 m panel show the PV cuts presented in Figure 12. Bottom panel: the full and dashed contours show the redshifted and blueshifted SiO(5–4) outflow emission, respectively. All the SiO emission contour levels start at 4σ and continue in steps of 2σ. The σ value for each outflow emission is shown in the respective map in mJy beam^{-1}, except for the 30 m data only map which has units of K km s^{-1}. The dotted contours are the negative features due to the missing flux with the same contour levels as the positive ones in each panel. The synthesized beam of the outflow images is shown in the bottom left corner of each panel. The (0, 0) point in each panel is R.A. 02^{h}25^{m}40^{s}.68, decl. +62°05′51″.5 (J2000).

(A color version of this figure is available in the online journal.)

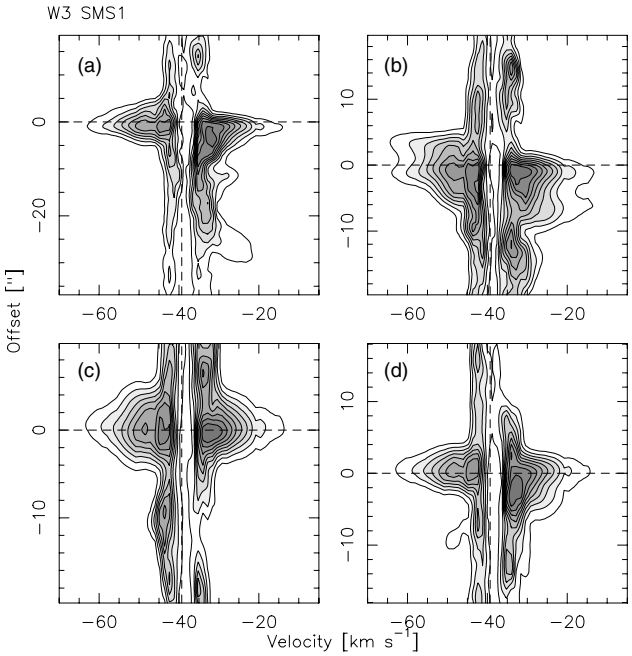

Figure 12. Position–velocity diagrams of W3 SMS1 for the ^{12}CO SMA+30 m outflow observations with a velocity resolution of 1.2 km s^{-1}. The PV cut of each panel is shown in the top middle panel of Figure 11 as the same letters a, b, c and d. The contour levels are from 10% to 90% from the peak emission (30.3 Jy beam^{-1} for panel (a), 26.6 Jy beam^{-1} for panel (b), 28.3 Jy beam^{-1} for panel (c), 31.4 Jy beam^{-1} for panel (d)) in steps of 10%. The $v_{\rm lsr}$ at −39.3 km s^{-1} and the central position are marked by vertical and horizontal dashed lines. The central position of panels (a) and (b) is the SMS1-MM1 source, and for panels (c) and (d) it is the redshifted outflow peak at R.A. 02^{h}25^{m}40^{s}.61, decl. +62°05′51″.7 (J2000).

while another blueshifted lobe resembles the Hubble law with increasing velocity at a larger distance from the outflow center (Arce et al. 2007).

Ridge & Moore (2001) found a bipolar outflow associated with W3 SMS1 in the direction NW–SE. The redshifted emission of this outflow peaks toward SMS1 but the blueshifted emission extends toward SMS2. We do not detect this outflow; however, we do detect outflows in SMS2 (Figure 13). Although the redshifted emission is not as strong as the blueshifted emission, it is prominent enough to show that the outflow is associated with SMS2-MM2. We believe that the blueshifted outflow emission (Ridge & Moore 2001) detected is driven by SMS2-MM2 not SMS1-MM1 (aka W3 IRS5). Furthermore, there is a ∼4 km s^{-1} difference between SMS1 and SMS2. One could easily mistake the CO emission at the $v_{\rm lsr}$ of SMS2 as blueshifted outflow emission.

W3 SMS3. Figure 15 shows the combined SMA and 30 m outflow images of W3 SMS3. All panels exhibit strong blueshifted emission associated with SMS2. Some weak redshifted and blueshifted features are detected toward SMS3, but we do not find any outflow signature associated with SMS3. Perhaps the outflow activity is weak at SMS3, and due to the interference from the strong emission at SMS2, we cannot recover the outflow emission. This again indicates that SMS3 is at an early evolutionary stage, with hardly any star formation activity.

3.4. Rotational Structures

We use $SO_2(22_{7,15}–23_{6,16})$, $H_2CO(3_{0,3}–2_{0,2})$, H30α, $CH_3OH(4_{2,2}–3_{1,2})$E, and HC_3N(24–23) to study the rotational

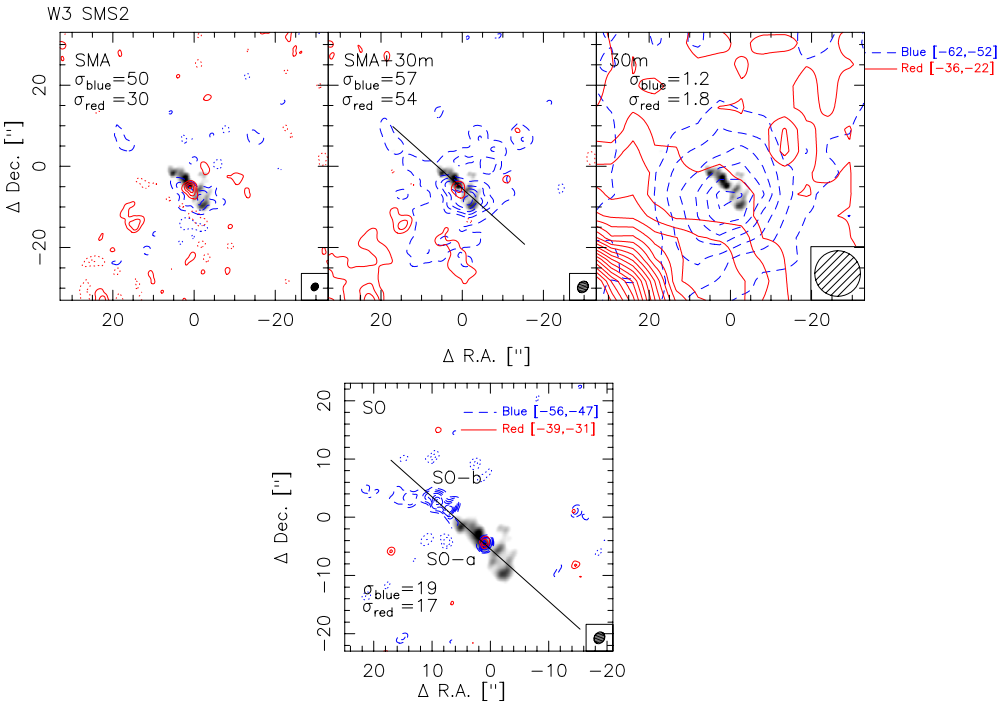

Figure 13. W3 SMS2 outflow images observed with the SMA and IRAM 30 m telescope. The gray scale in all panels is the SMA 1.3 mm continuum image. Top panels: the full and dashed contours show the redshifted and blueshifted ^{12}CO(2–1) outflow emission. The top left panel presents the SMA data only map, the middle one is the combined SMA+30 m data, and the right one is the IRAM 30 m data only map. The velocity-integration regimes are shown in the top right. All the ^{12}CO emission contour levels start at 4σ, for the blueshifted outflow the contour step is 8σ and for the redshifted outflow it is 4σ. Bottom panel: the full and dashed contours show the redshifted and blueshifted SO(6_5–5_4) outflow emission. All the SO emission contour levels start at 4σ and continue in steps of 2σ. The solid lines in the SMA+30 m panel and the SO panel show the PV cuts presented in Figure 14. The σ value for each outflow emission is shown in the respective map in mJy beam^{-1}, except for the 30 m data only map which has units of K km s^{-1}. The dotted contours are the negative features due to the missing flux with the same contour levels as the positive ones in each panel. The synthesized beam of the outflow images is shown in the bottom right corner of each panel. The (0, 0) point in each panel is R.A. $02^{h}25^{m}31\overset{s}{.}22$, decl. $+62°06'25\overset{''}{.}52$ (J2000).

(A color version of this figure is available in the online journal.)

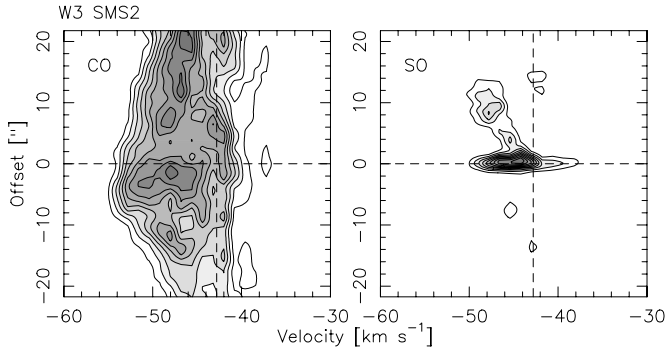

Figure 14. Position–velocity diagram of W3 SMS2 for the ^{12}CO(2−1) SMA+30 m data and the SO data observations with a velocity resolution of 1.2 km s^{-1}. The PV cut is in the NE–SW direction with a P.A. of ∼50° E of N (the cut is shown in Figure 13). The contour levels are from 10% to 90% from the peak emission (16.9 Jy beam^{-1} for the CO panel and 2.6 Jy beam^{-1} for the SO panel) in steps of 10%. The $v_{\rm lsr}$ at −42.8 km s^{-1} and the central position (i.e., the SMS2-MM2 peak position) are marked by vertical and horizontal dashed lines.

properties of the three regions. We find rotation structures in SMS1 and SMS2, and do not find any rotational signatures in SMS3.

W3 SMS1. In the velocity map of $SO_2(22_{7,15}$–$23_{6,16})$; Figure 16), we see a clear velocity gradient in the northwest–southeast (NW–SE) direction, which is perpendicular to the direction of outflow-a (Figure 11), indicating that the envelope of SMS1-MM1 may rotate in this direction. Rodón et al. (2008) also observed a similar velocity gradient from a lower sulfur dioxide transition. The $H_2CO(3_{0,3}$–$2_{0,2})$ velocity map (Figure 16) shows a larger structure with complicated velocity signatures.

The H30α velocity map (Figure 16) shows a velocity gradient in the NE–SW direction and follows the distribution of the compact radio sources detected by Tieftrunk et al. (1997), which is nearly perpendicular to the direction of outflow-b. Hence, the H30α emission could be tracing the rotation of the ionized gas, although we cannot exclude the possibility of an ionized jet. This velocity gradient is different from the one seen in $SO_2(22_{7,15}$–$23_{6,16})$, and outflow-d is found in the similar direction but with an inverse red–blue signature (Figure 11).

The PV diagrams of the $SO_2(22_{7,15}$–$23_{6,16})$, $H_2CO(3_{0,3}$–$2_{0,2})$, and H30α emission are shown in Figure 17. The corresponding PV cuts of each panel are shown in Figure 16. The PV diagrams of $SO_2(22_{7,15}$–$23_{6,16})$ and $H_2CO(3_{0,3}$–$2_{0,2})$ show that the rotational structure is not in Keplerian motion, hence it may be just a rotating and infalling core similar to the toroids or envelope described by Cesaroni et al. (2007). The rotational envelope detected by our $SO_2(22_{7,15}$–$23_{6,16})$ observation has a size of $\sim 10^4$ AU at the given distance of 1.95 kpc. This indicates that the proto-Trapezium system shares one common rotating envelope. The velocity jump found by Rodón et al. (2008) in SO_2 emission is also confirmed by our H_2CO observations.

The PV diagram of the H30α emission shows quite a small velocity gradient for the radio recombination line. We extract the spectrum toward the emission peak in Table 4, and derive the FWHM line width from the Gaussian fitting as ∼9.2 km s^{-1}. For a typical HCH II region with a temperature of 8000 K, the

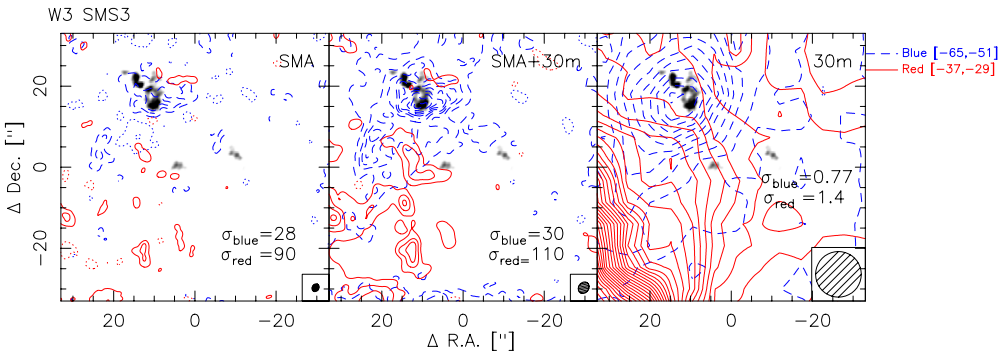

Figure 15. W3 SMS3 outflow images observed with the SMA and IRAM 30 m telescope. The gray scale in all panels is the SMA 1.3 mm continuum image. The full and dashed contours show the redshifted and blueshifted ^{12}CO(2–1) outflow emission. The top left panel presents the SMA data only map, the middle one is the combined SMA+30 m data, and the right one is the IRAM 30 m data only map. The velocity-integration regimes are shown in the top right. All the ^{12}CO emission contour levels start at 4σ, for the blueshifted outflow the contour step is 8σ and for the redshifted outflow it is 4σ. The σ value for each outflow is shown in the respective map in mJy beam^{-1}, except for the 30 m data only map which has units of K km s^{-1}. The dotted contours are the negative features due to the missing flux with the same contour levels as the positive ones in each panel. The synthesized beam of the outflow images is shown in the bottom right corner of each panel. The (0, 0) point in each panel is R.A. 02^{h}25^{m}29^s.49, decl. +62°06′00″.6 (J2000).

(A color version of this figure is available in the online journal.)

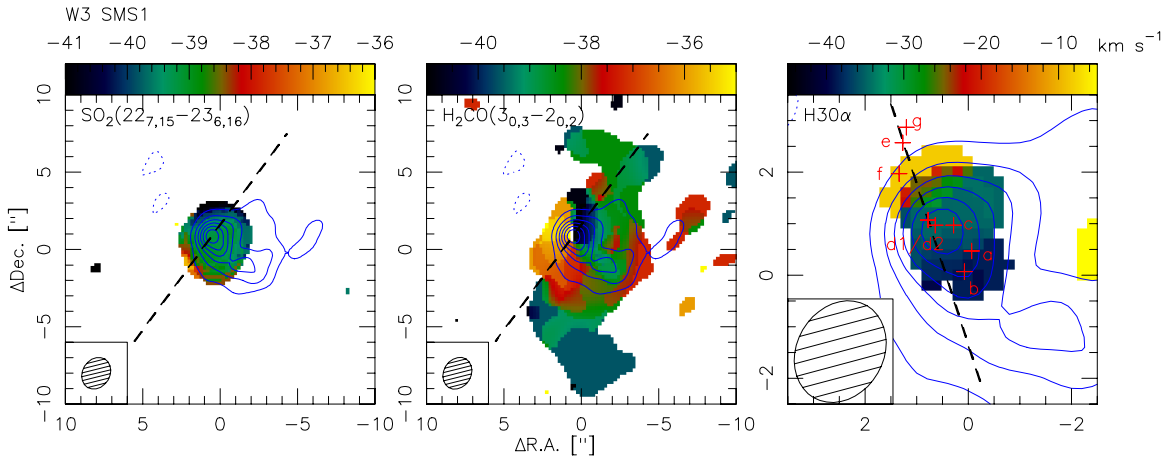

Figure 16. $SO_2(22_{7,15}–23_{6,16})$, $H_2CO(3_{0,3}–2_{0,2})$, and H30α velocity (first) moment maps overlaid with the SMA 1.3 mm dust continuum of W3 SMS1. The contours start at 5σ and increase in steps of 5σ in all panels (1σ = 3.6 mJy beam^{-1}). The dotted contours are the negative features due to the missing flux with the same contour levels as the positive ones in each panel. The dashed lines in each panel show the PV diagram cuts presented in Figure 17. The crosses and the letters mark the compact radio sources detected by Claussen et al. (1994) and Tieftrunk et al. (1997). All moment maps are clipped at the 5σ level of the respective line channel map. The synthesized beams of the moment maps are shown in the bottom left corner of each plot. The (0, 0) point in each panel is R.A. 02^{h}25^{m}40^s.68, decl. +62°05′51″.5 (J2000).

(A color version of this figure is available in the online journal.)

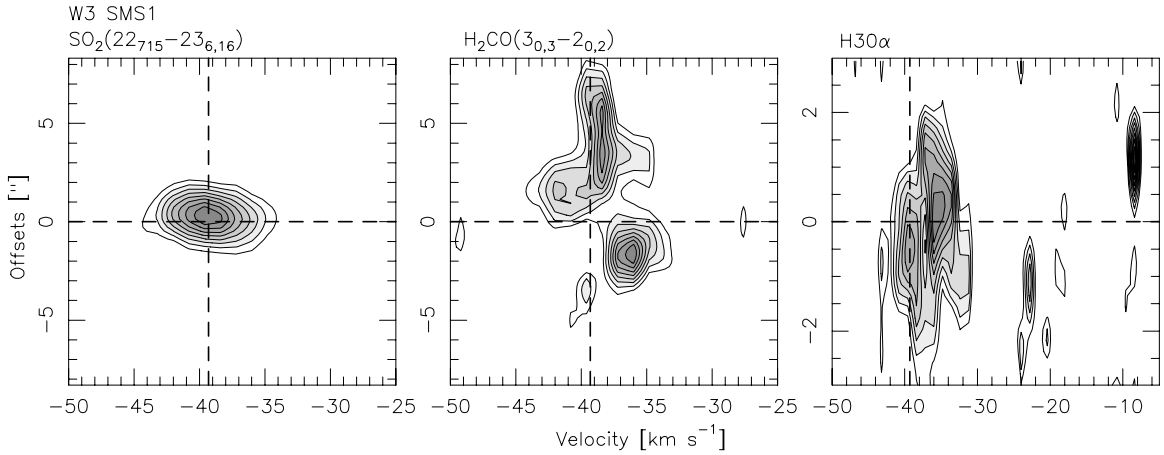

Figure 17. Position–velocity diagrams derived for the cuts along the observed velocity gradient in Figure 16 with a velocity resolution of 1.2 km s^{-1}. The PV cut for H30α and $SO_2(22_{7,15}–23_{6,16})$ is marked in the corresponding first moment maps (Figure 16). The PV cuts for $H_2CO(3_{0,3}–2_{0,2})$ a and b are shown as lines a and b in the $H_2CO(3_{0,3}–2_{0,2})$ velocity map (Figure 16). All the contour levels are from 10% to 90% of the peak emission (264 mJy beam^{-1} for H30α, 833 mJy beam^{-1} for $H_2CO(3_{0,3}–2_{0,2})$ panel (a), 525 mJy beam^{-1} $H_2CO(3_{0,3}–2_{0,2})$ panel (b), 2.68 Jy beam^{-1} for $SO_2(22_{7,15}–23_{6,16})$) in steps of 10%. The offsets refer to the distance along the cuts from the dust continuum peak of SMS1-MM1. The $v_{\rm lsr}$ at −39.3 km s^{-1} and the central position (the SMS1-MM1 continuum peak) are marked by vertical and horizontal dashed lines.

Table 4
CH_3CN, CH_3OH, and H30α Peak Positions

Lines	R.A. (J2000)	Decl. (J2000)
$CH_3CN(k = 1, 2)$	2:25:40.54 ± 0.02	+62:05:50.9 ± 0.3
$CH_3OH(4_{2,2}–3_{1,2})E$	2:25:40.47 ± 0.01	+62:05:51.0 ± 0.2
H30α[a]	2:25:40.68 ± 0.03	+62:05:51.7 ± 0.5

Note. [a] We only fitted the peak at SMS1-MM1.

line width due to thermal broadening would be 19.1 km s^{-1}. Hence, the H30α emission is likely tracing the gas associated with kinematic properties, e.g., rotation and/or outflow, but we cannot properly differentiate among the options.

W3 SMS2. In the velocity map of $CH_3OH(4_{2,2}–3_{1,2})E$ (Figure 18), we see a clear velocity gradient in the NE–SW direction, which is in a similar direction as the blueshifted outflow SO-b (bottom panel, Figure 13). CH_3OH is well known as a molecule that traces shocks, cores, and masers in star-forming regions (Beuther et al. 2005a; Jørgensen et al. 2004; Sobolev et al. 2007), therefore, we propose that this velocity gradient traces the near side of outflow SO-b. Another velocity gradient that is in the NW–SE direction is shown in both the $CH_3OH(4_{2,2}–3_{1,2})E$ and HC_3N(24–23) velocity maps (Figure 18). This velocity gradient is also perpendicular to the direction of outflow SO-b (bottom panel, Figure 13). CH_3OH and HC_3N are well-known low-mass disk tracers (e.g., Goldsmith et al. 1999), hence the NW–SE velocity gradient suggests a rotational structure.

The PV diagrams of the $CH_3OH(4_{2,2}–3_{1,2})E$ and HC_3N(24–23) emission are shown in Figure 19. The PV cut of $CH_3OH(4_{2,2}–3_{1,2})E$ goes through the SMS2-MM2 dust continuum peak and is marked as line a in Figure 18. The PV diagram shows that the blueshifted $CH_3OH(4_{2,2}–3_{1,2})E$ resembles the outflow Hubble law with increasing velocity at a larger distance from the outflow center (Arce et al. 2007). The PV cuts of $CH_3OH(4_{2,2}–3_{1,2})E$ (panel (b)) and HC_3N(24–23) are shown in Figure 18 (line b in the $CH_3OH(4_{2,2}–3_{1,2})E$ panel and the line in HC_3N(24–23) panel) are perpendicular to line a (the direction of the outflow SO-b). These two PV diagrams show that the rotational structure is not in Keplerian motion. With a size of ∼6300 AU (d = 1.95 kpc), this structure is similar to the rotational structure described in Wang et al. (2011) and Fallscheer et al. (2009), i.e., a large-scale structure with a non-Keplerian velocity gradient. We do not find a rotational structure for SMS2-MM1, and no rotational signature is found in SMS3 either.

3.5. Temperature Determinations

The dense gas ($n \gtrsim 10^5$ cm^{-3}) tracer CH_3CN can be used as a temperature determinator (e.g., Loren & Mundy 1984). For W3 SMS1, four $k = 0 \ldots 3$ lines of the $CH_3CN(12_k–11_k)$ ladder were detected and they do not peak on any of the SMA continuum sources, so a spectrum was extracted toward the CH_3CN integrated emission peak with only the compact configuration data. For W3 SMS2, seven $k = 0 \ldots 6$ lines of the $CH_3CN(12_k–11_k)$ ladder were detected and they all peak on the SMA continuum source SMS2-MM2, so we extract a spectrum toward the SMS2-MM2 continuum peak with only the compact configuration data. Both spectra are shown in Figure 20. We assume local thermodynamic equilibrium (LTE) and optically thin emission, and construct the rotational diagrams following the method outlined in Appendix B of Zhang et al. (1998a). The level populations $N_{j,k}$ were calculated from the Gaussian fitting results of the spectra shown in Figure 20. The derived

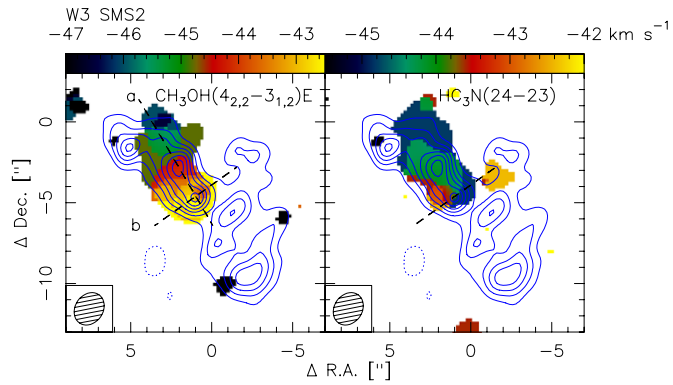

Figure 18. $CH_3OH(4_{2,2}–3_{1,2})E$ and HC_3N(24–23) velocity (first) moment maps overlaid with the SMA 1.3 mm dust continuum of W3 SMS2. The contours start at 5σ and increase in steps of 5σ in all panels (σ = 2.5 mJy beam^{-1}). The dotted contours are the negative features due to the missing flux with the same contour levels as the positive ones in each panel. The dashed lines in each panel show the PV diagram cuts presented in Figure 19. All moment maps were clipped at the 5σ level of the respective line channel map. The synthesized beams of the moment maps are shown in the bottom left corner of each plot. The (0, 0) point in each panel is R.A. 02^{h}25^{m}31^s.22, decl. +62°06′25″.52 (J2000).

(A color version of this figure is available in the online journal.)

rotational diagrams are shown in Figure 21, along with the linear fit of all the detected k components which gives the value of T_{rot} ∼ 116 ± 46 K for SMS1 and ∼140 ± 30 K for SMS2-MM2. Studies of Wilner et al. (1994) revealed that T_{rot} derived with this method agrees well with those obtained from the large velocity gradient (LVG) calculations. The average line width of the $CH_3CN(12_k–11_k)$ spectra toward SMS1 (top panel, Figure 20) is ∼1.6 km s^{-1}. Considering that our spectral resolution is 1.2 km s^{-1}, the line width is not fully resolved. For a temperature of ∼116 K, the thermal line width of CH_3CN is ∼0.36 km s^{-1}. For hot cores with temperatures of ∼100 K, the average CH_3CN line width is $\gtrsim$5 km s^{-1} (Zhang et al. 1998a, 2007; Wang et al. 2011). Even for some IRDCs the line width is still $\gtrsim$2.8 km s^{-1} (Beuther & Sridharan 2007). All these features indicate that the gas from which the CH_3CN emission originated is warm and at the same time shows a low level of turbulence. To our knowledge, this has rarely (or not at all) been seen before.

H_2CO is a well-known kinetic temperature determinator (e.g., Mangum & Wootten 1993; Jansen et al. 1994; Mühle et al. 2007; Watanabe & Mitchell 2008). Since it is a slightly asymmetric rotor, transitions between energy levels with different K are only collisionally excited. Therefore, comparing the level populations with different K components from the $\Delta J = 1$ transitions gives an estimate of the kinematic temperature of the medium (Mangum & Wootten 1993). The spectra of $H_2CO(3_{0,3}–2_{0,2})$ and $H_2CO(3_{2,2}–2_{2,1})$ were extracted toward the continuum peaks of SMS1-MM1/2 and SMS2-MM1/2/3/7 with the compact configuration data. The spectra were processed with CLASS and are shown in Figure 22. We assume LTE and optically thin emission, and calculate the temperature T_{kin} of these sources following the method described by Mangum & Wootten (1993). The temperature results are shown in Table 5. The high temperature of SMS2-MM7 (98 ± 33 K) could be due to the fact that it is heated by the nearby infrared source IRS4-a (Figure 3).

Despite the possibility that the H_2CO emission is not really optically thin and it might be affected by the missing flux, the T_{kin} we obtain from the H_2CO intensity ratio agrees quite well with the T_{rot} we obtain from the $CH_3CN(12_k–11_k)$ line fit for SMS1. The CH_3CN and CH_3OH integrated intensity maps (Figure 5) indicate that SMS1-MM2 has a higher temperature than SMS1-

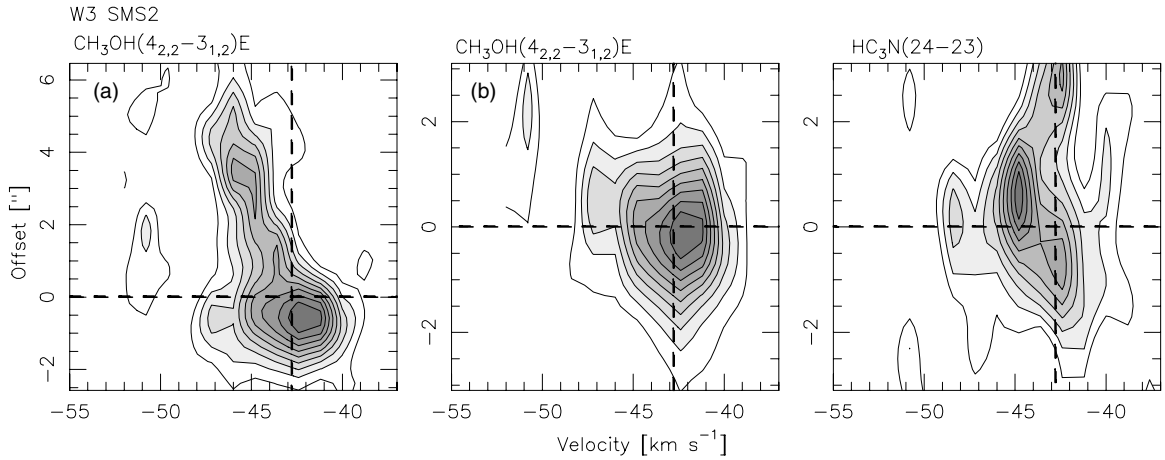

Figure 19. Position–velocity diagrams derived for the cuts along the observed velocity gradient in Figure 18 with a velocity resolution of 1.2 km s^{-1}. The PV cuts for the left and middle panels are marked as lines a and b in the $CH_3OH(4_{2,2}–3_{1,2})E$ velocity map, respectively (Figure 16). The PV cut for HC_3N(24–23) is marked as the straight line in its first moment map (Figure 18). All the contour levels are from 10% to 90% of the peak emission (from left to right, 621, 644, and 370 mJy $beam^{-1}$, respectively) in steps of 10%. The offsets refer to the distance along the cuts from the dust continuum peak of SMS2-MM2. The v_{lsr} at −42.8 km s^{-1} and the central position (i.e., the SMS2-MM2 peak position) are marked by vertical and horizontal dashed lines.

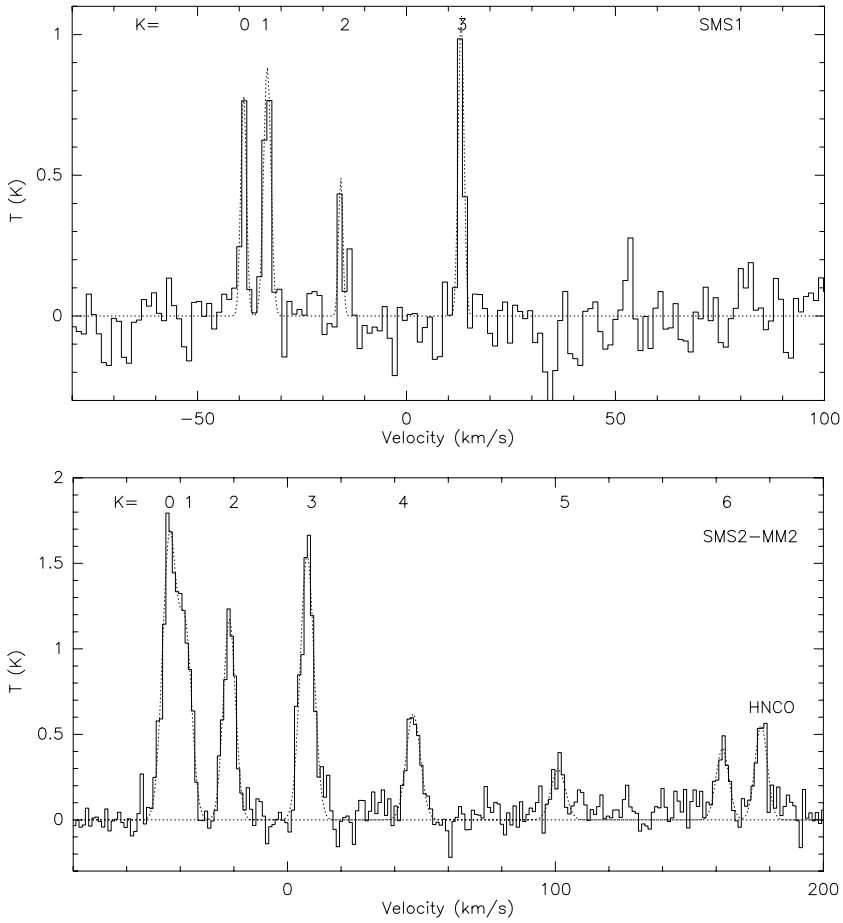

Figure 20. Observed $CH_3CN(12_k–11_k)$ spectrum toward the CH_3CN integrated intensity peak in SMS1 (top panel) and continuum peak SMS2-MM2 (bottom panel) with only the compact configuration data. The dotted line shows the best Gaussian fit obtained with CLASS for the lines.

MM1, and this is supported by the T_{kin} we obtain from the H_2CO intensity ratio.

The LVG model calculations done by Mangum & Wootten (1993) show that temperatures determined from the $H_2CO(3_{0,3}–2_{0,2})$ and $H_2CO(3_{2,2}–2_{2,1})$ line intensity ratios have a large dispersion depending on the volume density where the line ratio is less than 3.5, which corresponds to a temperature of 70 K. Since we do not have the volume density information for our continuum sources, the temperature determination can only be done between 20 and 70 K for line ratios larger than 3.5. Therefore, the T_{kin} we obtain for SMS2-MM2 is not reliable. Nevertheless, the temperature we obtain from the CH_3CN and H_2CO measurements confirms the hot molecular core (HMC) nature of the continuum source SMS2-MM2.

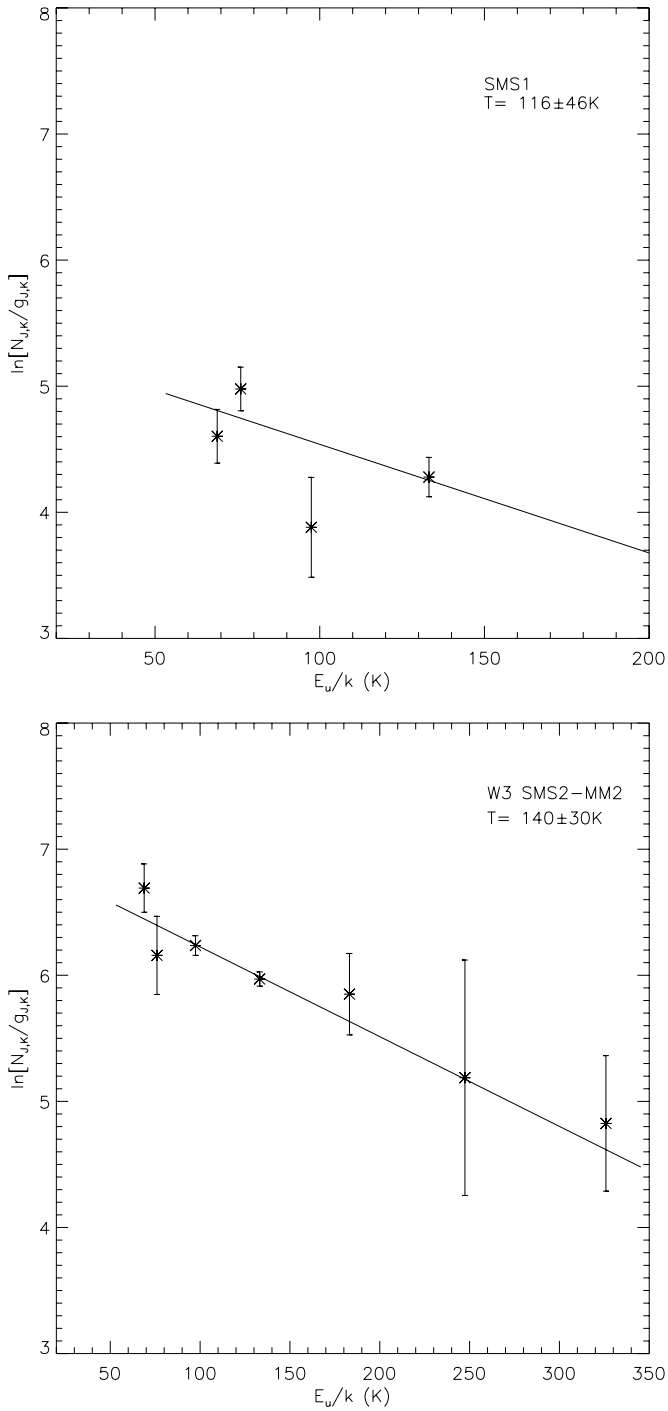

Figure 21. LTE rotational diagrams of the $CH_3CN(12_k–11_k)$ lines shown in Figure 20. The solid line is the linear fit to all the k components calculated following Equation (B6) from Zhang et al. (1998a).

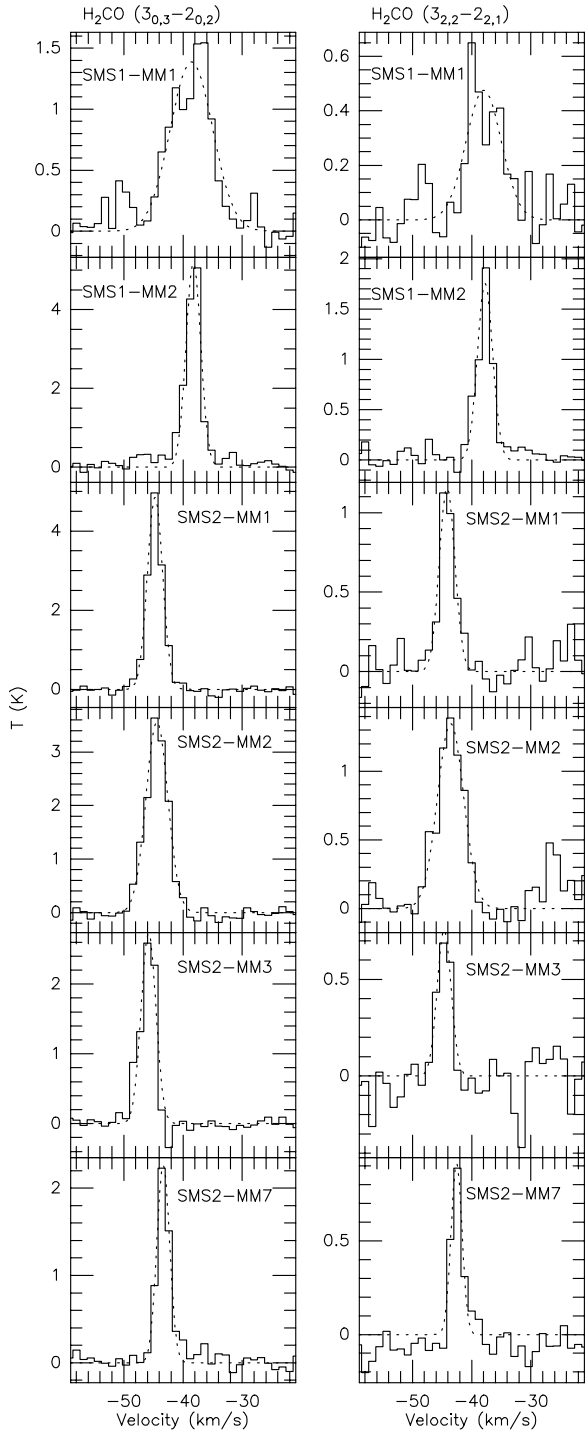

Figure 22. H_2CO spectra toward the SMA 1.3 mm continuum sources SMS1-MM1/2 and SMS2-MM1/2/3/7 with only the compact configuration data. The dotted lines show the Gaussian fit obtained with CLASS for each spectrum.

4. DISCUSSION

4.1. Different Evolutionary Stages of the Continuum Sources

The SMA and IRAM 30 m data together reveal three massive star formation regions in different evolutionary stages. With our high-resolution SMA observations (∼2900 AU at the given distance of 1.95 kpc), we find that all SCUBA continuum sources fragment into several cores.

W3 SMS3 is considered to be the youngest region since no radio or infrared sources are found here (Megeath et al. 2008). Our results also support this, in particular the low number of molecular lines and the absence of outflow emission. The large amount of continuum flux filtered out in our observations indicates that the gas in this region is relatively uniformly distributed. VLA observations of $NH_3(1,1)$ and $NH_3(2,2)$ found extended emission toward SMS3, and furthermore, this extended emission was resolved into four NH_3 clumps surrounding the core emission toward SMS3 (Tieftrunk et al. 1998). Our continuum source SMS3-MM2 is associated with the main NH_3 core, and MM1 and MM3 are associated with one of the compact NH_3 clumps, clump 4 (Tieftrunk et al. 1998). From the line width of the single-

Table 5
Temperature Estimation Results for SMS1 and SMS2

Source	T_{rot}[a] (K)	T_{kin}[b] (K)	$\int T_b(H_2CO(3_{0,3}-2_{0,2}))dv$ / $\int T_b(H_2CO(3_{2,2}-2_{2,1}))dv$
SMS1-MM1	...	71 ± 18	3.5
SMS1-MM2	116 ± 46[c]	101 ± 16	2.9
SMS2-MM1	...	57 ± 6	4.1
SMS2-MM2	140 ± 30	231 ± 97	2.2
SMS2-MM3	...	62 ± 14	3.8
SMS2-MM7	...	98 ± 33	2.9

Notes.
[a] T_{rot} is obtained from the rotational diagram of the CH_3CN lines.
[b] T_{kin} is obtained from the H_2CO line intensity ratios.
[c] The spectrum we use to estimate this temperature is extracted from the CH_3CN emission peak, which is close to SMS1-MM2, so we put this number here.

dish $^{13}CO(2–1)$ data (∼4.9 km s^{-1}), following the equation described in Pillai et al. (2006), we estimate the virial mass for SMS3 as ∼1563 $M_\odot$, which is much larger than the virial mass Tieftrunk et al. (1998) obtained (300–400 $M_\odot$) from the NH_3 observations and the mass we obtain from the SCUBA measurements (Table 1). Our ^{13}CO line may not be completely optically thin, and traces more or less all of the molecular gas, including the more diffuse envelope, whereas the NH_3 and SCUBA trace the dense gas in the center. Therefore, the NH_3 virial mass Tieftrunk et al. (1998) obtained should better represent the mass from SCUBA. Hence, SMS3 is approximately in virial equilibrium. Since the peak column density (Table 1) is also above the proposed threshold for high-mass star formation of 1 g cm^{-2} (Krumholz & McKee 2008), we infer that SMS3 is at a very early stage of massive star formation.

For the more evolved regions SMS1 and SMS2, both harbor NIR clusters (Ojha et al. 2004; Bik et al. 2011) and HCH II regions (Tieftrunk et al. 1997), and both show strong signatures of active star-forming activity. However, the continuum subsources in these two regions all show different evolutionary features.

Evolutionary sequence in SMS1. Our high-resolution observations show a more complicated picture. Most of the molecular lines, especially some high excitation energy level sulfur-bearing molecular lines, peak on the strongest continuum source SMS1-MM1, which is associated with the HCH II region cluster W3 M and infrared source IRS5. Rodón et al. (2008) resolved SMS1-MM1 into four 1.4 mm continuum sources. Combining the strong outflows we find here, we can confirm that a massive multiple system is forming in SMS1-MM1. The fact that SMS1-MM2 is not associated with any NIR point sources and has far fewer lines than SMS1-MM1 is consistent with a starless core. The high temperature of SMS1-MM2 we estimate (Table 5) might be due to the shock heating caused by the outflows driven by SMS1-MM1 (Figure 11). SMS1-MM4 shows almost no lines aside from the three CO isotopologues, and it is also associated with an NH_3 core detected by Tieftrunk et al. (1998). Therefore, we conclude that SMS1-MM4 might be at a very early evolutionary stage and a potential starless core. Since SMS1-MM4 is in the direction of the redshifted component of outflow-b and there is SiO emission nearby, it might be a swept-up ridge by the outflow.

Evolutionary sequence in SMS2. Tieftrunk et al. (1998) found a filamentary structure traced in NH_3 starting at the HCH II region W3 Ca and extending toward the NE. Our SMA observations not only recover part of the filament but also detect continuum emission toward the UCH II region W3 C, which is the most evolved source in SMS2. Most lines detected in SMS2 peak on the SMA continuum source SMS2-MM2, which is associated with the HCH II region W3 Ca (Tieftrunk et al. 1997). We also detect outflows toward SMS2-MM2. The infrared source IRS4 detected by Wynn-Williams et al. (1972) consists of two infrared sources, which are IRS4-a and IRS4-b (Figure 3). IRS4-a was classified as an O8-B0.5V star, and is considered to be the exciting source of the UCH II region W3 C (Bik et al. 2011). The other IR source IRS4-b is associated with the SMA continuum source SMS2-MM2 and the HCH II region, and it also dominates the mid- and far-infrared emission. All these features show that SMS2-MM2 is in the hot core evolutionary stage. It is surprising that the strongest continuum source in this region, SMS2-MM1, shows only a few molecular lines and is in a younger evolutionary stage as a potential massive starless core. Last but not least, SMS2-MM3 and SMS2-MM7 exhibit fewer lines than SMS2-MM1 (Table 6) and have strong DCN emission (Figure 7), which makes them the youngest sources in SMS2. All these continuum sources show clear evolutionary stages from the most evolved UCH II region to potential starless cores within 30,000 AU.

In summary, at large scales, the whole W3 Main region harbors the relatively evolved H II regions W3 A, W3 H, and W 3 D (Figure 2), and a young cluster is forming inside. Our observations reveal three massive star-forming subregions in different evolutionary stages. W3 SMS3 is in the youngest evolutionary stage, while W3 SMS1 and W3 SMS2 are more evolved. Furthermore, within the subregions, we find the SMA continuum sources in different evolutionary stages, from potential starless cores to typical high-mass hot cores. The data clearly show that the age difference of massive star formation regions not only exists on clump scales, but also within the clump.

4.2. Astrochemistry

Chemistry can be used to determine the evolutionary stages of massive star-forming regions. The continuum sources show different chemical evolutionary stages. SMS2-MM2 shows typical HMC chemical characteristics, with many hot/dense gas tracer emission, e.g., CH_3OH and CH_3CN lines (Figure 7). The ^{13}CS and DCN emission offset from SMS2-MM2 also shows its HMC nature, since in a high temperature environment (∼100 K), CS quickly reacts with OH forming SO and SO_2 (Beuther et al. 2009), and DCN can be destroyed rapidly by reaction with atomic hydrogen (Wright et al. 1996; Hatchell et al. 1998). For the younger sources, i.e., the potential starless cores, DCN and ^{13}CS lines are also useful to determine evolutionary stages.

DCN is reported as a indicator of the evolution of the dense cores, as it is liberated from the evaporated grain mantle and could be destroyed rapidly in the hot gas by reaction with atomic hydrogen (Wright et al. 1996; Hatchell et al. 1998). The ratio of DCN/HCN is often used to determine the evolutionary stage of high-mass cores. Since we do not have the HCN observations, we cannot get this ratio to constrain the exact evolutionary stages of the sources; however, the detection/non-detection of DCN provides us with a clue about the evolution. We detect DCN emission toward SMS2-MM1/3/7 and SMS3-MM2, which indicates that these four continuum sources are in an early evolutionary stage. The non-detection of DCN toward the starless cores SMS1-MM2 and SMS1-MM4 could be due to the fact that the jets driven by SMS1-MM1 heated the ambient gas and destroyed the DCN molecules. We do not detect DCN

Table 6
Observed Lines at All Continuum Peaks

ν	Transition	$E_{\rm lower}$	SMS1				SMS2							SMS3		
(GHz)		(K)	MM1	MM2	MM3	MM4	MM1	MM2	MM3	MM4	MM5	MM6	MM7	MM1	MM2	MM3
							LSB									
217.105	SiO(5–4)	21	√	√		√										
217.239	DCN(3–2)	10					√		√				√		√	
217.830	^{33}SO($5_{6,6}$–$4_{5,5}$)	24	√	√												
218.222	$H_2CO(3_{0,3}–2_{0,2})$	10	√	√			√	√	√				√			
218.325	HC_3N(24–23)	121	√				√	√								
218.440	$CH_3OH(4_{2,2}–3_{1,2})$E	35		√			√	√						√	√	√
218.476	$H_2CO(3_{2,2}–2_{2,1})$	58	√	√			√	√	√							
218.760	$H_2CO(3_{2,1}–2_{2,0})$	58	√	√			√	√								
218.903	OCS(18–17)	89	√	√				√								
219.276	$SO_2(22_{7,15}–23_{6,16})$	394	√	√												
219.355	$^{34}SO_2(11_{1,11}–10_{0,10})$	50	√	√												
219.466	$SO_2(v_2 = 1)(22_{2,20}–22_{1,21})$	983	√													
219.560	$C^{18}O$(2–1)	5.3	√	√		√	√	√	√	–		–	√	√	√	√
219.798	$HNCO(10_{0,10}–9_{0,9})$	48	√	√				√								
219.949	$SO(6_5–5_4)$	24	√	√		√	√	√	√				√	√	√	√
220.079	$CH_3OH(8_{0,8}–7_{1,6})$E	85		√				√								
220.165	$SO_2(v_2 = 1)(16_{3,14}–16_{2,14})$	613	√													
220.399	^{13}CO(2–1)	5.3	√	√	√	√	√	√	√	–	√	√	√	√	√	√
220.585	$HNCO(10_{1,9}–9_{1,8})$	91	√					√								
220.594	$CH_3CN(12_6–11_6)$	315						√								
220.620	$^{33}SO_2(11_{1,11}–10_{0,10})$	50	√													
220.641	$CH_3CN(12_5–11_5)$	237						√								
220.679	$CH_3CN(12_4–11_4)$	173						√								
220.709	$CH_3CN(12_3–11_3)$	123		√			√	√								
220.730	$CH_3CN(12_2–11_2)$	87		√				√								
220.743	$CH_3CN(12_1–11_1)$	65		√				√								
220.747	$CH_3CN(12_0–11_0)$	58		√				√								
							USB									
229.348	$SO_2(11_{5,7}–12_{4,8})$	111	√	√				√								
229.545	$SO_2(13_{2,12}–13_{1,13})$	828	√													
229.759	$CH_3OH(8_{-1,8}–7_{0,7})$E	77		√			√	√								
229.858	$^{34}SO_2(4_{2,2}–3_{1,3})$	7.7	√	√												
230.027	$CH_3OH(3_{2,2}–4_{1,4})$E	28		√				√								
230.538	^{12}CO(2–1)	5.5	√	√	–	√	√	√	√	√	√	√	√	–	√	√
230.965	$SO_2(37_{10,28}–38_{9,29})$	881	√													
231.061	OCS(19–18)	100	√					√								
231.221	$^{13}CS(5_0–4_0)$	22		√			√		√					√	√	√
231.901	H30α		√		√					√	√	√				
231.981	$SO_2(14_{3,11}–14_{2,12})$	593	√													
232.266	$S^{18}O(5_6–4_5)$	37	√													
232.419	$CH_3OH(10_{2,8}–9_{3,7})$A +	154	√	√				√								
232.946	$CH_3OH(10_{-3,8}–11_{-2,10})$E	179						√								

Notes. "√" indicates that this transition is detected toward this continuum source. "–" indicates that the spectrum extracted toward this source shows a pure negative feature due to the missing flux problem.

toward SMS3-MM1 and SMS3-MM3 either, but ^{13}CS emission is detected toward these two sources, which indicates they are in a very early evolutionary stage, too.

SMS1-MM1 also shows HMC chemical characteristics, with many emission lines and all the SO, SO_2 isotopologues peaking on the continuum source (Figures 5 and 6). However, of the typical dense/warm gas tracers CH_3OH and CH_3CN, only very weak CH_3OH emission and no CH_3CN emission is detected toward the continuum peak (Figure 5). The offset peak of CH_3OH could be explained by the shock produced by the outflow, but we cannot explain why the CH_3CN peak is offset from the continuum peak.

Another puzzle is that CH_3OH lines show extended emission toward the area between very young sources SMS3-MM1 and SMS3-MM2 (Figure 9). These are peculiar chemical properties of the SMS3 region.

4.3. Sequential and Potential Triggered Star Formation

NIR imaging and spectroscopy studies by Bik et al. (2011) show an age spread of at least 2–3 Myr for the massive stars within the H II regions in W3 Main. X-ray studies by Feigelson & Townsley (2008) revealed a low-mass young stellar cluster with an age of >0.5 Myr and Ojha et al. (2004) obtained an age of the NIR cluster of 0.3–1 Myr from the K_s-band luminosity function. In contrast, the UCH II regions such as W3 C and W3 F only have an age of $\sim 10^5$ yr (Wood & Churchwell 1989; Churchwell 2002; Mottram et al. 2011; Davies et al. 2011), and our SMA continuum sources SMS1-MM1 and SMS2-MM2 which are

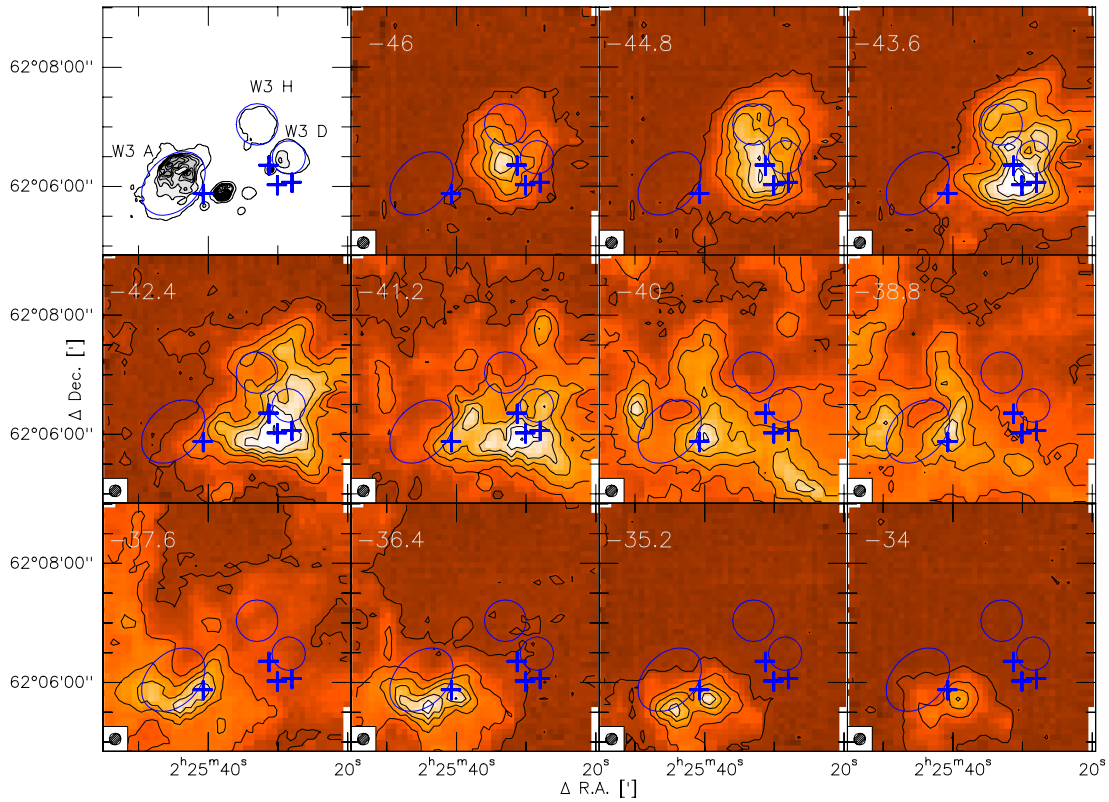

Figure 23. Single-dish ^{13}CO(2–1) channel map and the 6 cm VLA continuum image (Tieftrunk et al. 1997) of W3 Main. The top left panel shows the 6 cm VLA continuum image, and the contour levels start at 2.8 mJy beam^{-1} and continue in steps of 50 mJy beam^{-1}. The rest of the panels show the single-dish ^{13}CO(2–1) channel map with a spectral resolution of 1.2 km s^{-1}, with contour levels starting at 5σ and continuing in steps of 20σ (1σ = 0.35 K). The crosses mark the position of the SMA continuum sources SMS1-MM1, SMS2-MM2, SMS3-MM1, and SMS3-MM2. The three circles/ellipses outline the approximate position and size of the three H II regions, W3 A, H, and D (Tieftrunk et al. 1997). The beam of the single-dish data is shown in the bottom left corner of each panel.

(A color version of this figure is available in the online journal.)

associated with HCH II regions are even younger (few times 10^4 yr; Mottram et al. 2011; Davies et al. 2011). Furthermore, the potential starless cores in SMS3 are still at the onset of massive star formation. The age differences reveal different stellar populations. The OB stars associated with the diffuse H II regions and the low-mass cluster members are the first generation stars, and the exciting sources of the UCH II regions and our SMA continuum sources are the second generation stars. The second generation star formation might be triggered by the first generation stars or perhaps the star formation activities last over a prolonged period (Feigelson & Townsley 2008).

To investigate the interactions between the H II regions and the molecular cloud, we construct the single dish ^{13}CO(2–1) channel map (Figure 23). The channel map shows that the molecular cloud forms circle-like structures with velocity gradients around the H II regions W3 A, H, and D. For W3 A, in the panel −40 km s^{-1} of Figure 23, the molecular cloud forms a "ring" around W3 A with two main clumps located at the northeast and west of the H II region' s edge. These two main clumps move to the south a bit in the panel −38.8 km s^{-1}, but the "ring" is still there. In the panel −37 km s^{-1}, the "ring" is no longer present, and the clumps move to the south and join into one. Finally, in the panel −34 km s^{-1}, the clump moves to the southwest. These structures indicate a velocity gradient of the molecular cloud around the H II region W3 A from the north to the south. A similar velocity gradient is also found around the H II region W3 H, which starts in the panel −44.8 km s^{-1} and the direction is from the east to the southwest. For the H II region W3 D, a "ring" structure is found in the panel −43.6 km s^{-1} of Figure 23, and the clumps move south and east of W3 D in the next three channels. These velocity gradients suggest that the H II regions are expanding and interacting with the ambient molecular gas. Furthermore, the young stellar objects (YSOs) and potential starless cores of the SMS1, SMS2, and SMS3 regions are located close to the edge of the H II regions. These facts together indicate that the H II regions may have even triggered the star formation in these subregions.

Similar structures with molecular gas distributed as a ring structure have also been found around many H II regions or bubbles (Deharveng et al. 2009; Beaumont & Williams 2010; Fang et al. 2012).

In the S255 complex, Wang et al. (2011) revealed three massive star-forming regions with different evolutionary stages within the same region. Based on the age difference between the low-mass cluster and the central high-mass protostellar objects, they suggest that the low-mass stars form first under pressure of the H II regions sitting around them, and then the low- to intermediate-mass stars may enhance the instability of the central high-mass cores and may potentially have triggered the formation of the central high-mass stars. Unlike the symmetric geometry of the S255 complex, W3 Main is more randomly distributed.

SMS1 sits between W3 A and W3 B, and is also associated with the dense young stellar cluster (Feigelson & Townsley 2008; Megeath et al. 1996), which has the highest YSO density in W3 Main. The exciting source of W3 A has an age of

~3 Myr (Bik et al. 2011), and is much older than the NIR cluster (0.3–1 Myr, Ojha et al. 2004). Therefore, W3 A may trigger the formation of the NIR cluster and even the central high-mass stars (IRS5).

Tieftrunk et al. (1998) found a filament along the edge of W3 H and W3 D from NH_3 observations. Tieftrunk et al. (1998) suggested that this filament may be a swept-up layer of W3 H. As part of the filament, we suggest the SMA continuum sources in SMS2 may have formed under the influence of W3 D, and may even be triggered by W3 D in the dense gas at the head of the cometary H II region W3 D as discussed by Hoare et al. (2007). Additionally, we see an "age gradient," from the southwest to the northeast, with the objects getting younger and younger (Figure 2).

5. SUMMARY

Combining the single-dish IRAM 30 m observations and the high-resolution SMA observations, we characterize the different evolutionary stages of massive star formation regions within the W3 Main complex. W3 SMS1, SMS2, and SMS3 show varying dynamical and chemical properties, which indicate that they are in different evolutionary stages. Even within each subregion, massive cores with different evolutionary stages are found, e.g., in SMS2, the SMA continuum sources show evolutionary stages from the most evolved UCH II region to potential starless cores within 30,000 AU.

We find outflows in SMS1 and SMS2. The absence of an outflow in SMS3 indicates it is at the onset of massive star formation. The multiple outflows in SMS1 confirm that a multiple system is forming.

We detect 36 molecular lines in SMS1, 27 lines in SMS2, and 7 lines in SMS3. The temperature is determined from the CH_3CN *k*-ladder rotational diagram and H_2CO line intensity ratios for continuum sources in SMS1 and SMS2.

Rotational structures are found for SMS1-MM1 and SMS2-MM2, and in SMS1-MM1 we find a velocity gradient in the hydrogen recombination line H30α. This may trace rotation and/or outflow, but we cannot distinguish between these scenarios.

Evidence for potential interactions between the molecular cloud and the H II regions is found in the $^{13}CO(2–1)$ channel map, which may indicate triggered star formation.

We thank the anonymous referee for useful comments. We thank the observers at the SMA and 30 m telescopes. We thank Dr. Tieftrunck for providing the VLA continuum maps. Y.W. thanks the productive discussions with Dr. Min Fang. This work is supported by the NSFC 10873037 and 10921063, 10733030, China.

Facilities: SMA, IRAM:30m

REFERENCES

Arce, H. G., Shepherd, D., Gueth, F., et al. 2007, Protostars and Planets V, ed. B. Reipurth, D. Jewitt, & K. Keil (Tucson, AZ: Univ. Arizona Press), 245
Beaumont, C. N., & Williams, J. P. 2010, ApJ, 709, 791
Beltrán, M. T., Cesaroni, R., Neri, R., et al. 2004, ApJ, 601, L187
Beuther, H., Churchwell, E. B., McKee, C. F., & Tan, J. C. 2007, Protostars and Planets V, ed. B. Reipurth, D. Jewitt, & K. Keil (Tucson, AZ: Univ. Arizona Press), 165
Beuther, H., & Nissen, H. D. 2008, ApJ, 679, L121
Beuther, H., Schilke, P., Menten, K. M., et al. 2005a, ApJ, 633, 535
Beuther, H., Schilke, P., Sridharan, T. K., et al. 2002, A&A, 383, 892
Beuther, H., & Shepherd, D. 2005, in Cores to Clusters: Star Formation with Next Generation Telescopes, ed. M. S. N. Kumar, M. Tafalla, & P. Caselli (New York: Springer), 105
Beuther, H., & Sridharan, T. K. 2007, ApJ, 668, 348
Beuther, H., Zhang, Q., Bergin, E. A., & Sridharan, T. K. 2009, AJ, 137, 406
Beuther, H., Zhang, Q., Greenhill, L. J., et al. 2005b, ApJ, 632, 355
Beuther, H., Zhang, Q., Sridharan, T. K., & Chen, Y. 2005c, ApJ, 628, 800
Bik, A., Henning, T., Stolte, A., et al. 2012, ApJ, 744, 87
Campbell, M. F., Butner, H. M., Harvey, P. M., et al. 1995, ApJ, 454, 831
Cesaroni, R., Galli, D., Lodato, G., Walmsley, C. M., & Zhang, Q. 2007, Protostars and Planets V, ed. B. Reipurth, D. Jewitt, & K. Keil (Tucson, AZ: Univ. Arizona Press), 197
Cesaroni, R., Neri, R., Olmi, L., et al. 2005, A&A, 434, 1039
Charnley, S. B., Tielens, A. G. G. M., & Rodgers, S. D. 1997, ApJ, 482, L203
Choi, M., Evans, N. J., II, & Jaffe, D. T. 1993, ApJ, 417, 624
Churchwell, E. 2002, ARA&A, 40, 27
Claussen, M. J., Berge, G. L., Heiligman, G. M., et al. 1984, ApJ, 285, L79
Claussen, M. J., Gaume, R. A., Johnston, K. J., & Wilson, T. L. 1994, ApJ, 424, L41
Davies, B., Hoare, M. G., Lumsden, S. L., et al. 2011, MNRAS, 416, 972
Deharveng, L., Zavagno, A., Schuller, F., et al. 2009, A&A, 496, 177
Di Francesco, J., Johnstone, D., Kirk, H., MacKenzie, T., & Ledwosinska, E. 2008, ApJS, 175, 277
Fallscheer, C. 2010, PhD thesis, Univ. Heidelberg, Germany
Fallscheer, C., Beuther, H., Zhang, Q., Keto, E., & Sridharan, T. K. 2009, A&A, 504, 127
Fang, M., van Boekel, R., King, R. R., et al. 2012, A&A, 539, A119
Feigelson, E. D., & Townsley, L. K. 2008, ApJ, 673, 354
Gaume, R. A., & Mutel, R. L. 1987, ApJS, 65, 193
Gibb, A. G., Davis, C. J., & Moore, T. J. T. 2007, MNRAS, 382, 1213
Goldsmith, P. F., Langer, W. D., & Velusamy, T. 1999, ApJ, 519, L173
Harris, S., & Wynn-Williams, C. G. 1976, MNRAS, 174, 649
Hasegawa, T. I., Mitchell, G. F., Matthews, H. E., & Tacconi, L. 1994, ApJ, 426, 215
Hatchell, J., Millar, T. J., & Rodgers, S. D. 1998, A&A, 332, 695
Hildebrand, R. H. 1983, QJRAS, 24, 267
Hoare, M. G., & Franco, J. 2007, arXiv:0711.4912
Hoare, M. G., Kurtz, S. E., Lizano, S., Keto, E., & Hofner, P. 2007, Protostars and Planets V, ed. B. Reipurth, D. Jewitt, & K. Keil (Tucson, AZ: Univ. Arizona Press), 181
Imai, H., Kameya, O., Sasao, T., et al. 2000, ApJ, 538, 751
Jansen, D. J., van Dishoeck, E. F., & Black, J. H. 1994, A&A, 282, 605
Jørgensen, J. K., Hogerheijde, M. R., Blake, G. A., et al. 2004, A&A, 415, 1021
Krumholz, M. R., Klein, R. I., & McKee, C. F. 2007, ApJ, 656, 959
Krumholz, M. R., Klein, R. I., McKee, C. F., Offner, S. S. R., & Cunningham, A. J. 2009, Science, 323, 754
Krumholz, M. R., & McKee, C. F. 2008, Nature, 451, 1082
Kuiper, R., Klahr, H., Beuther, H., & Henning, T. 2010, ApJ, 722, 1556
Ladd, E. F., Deane, J. R., Sanders, D. B., & Wynn-Williams, C. G. 1993, ApJ, 419, 186
Loren, R. B., & Mundy, L. G. 1984, ApJ, 286, 232
Mangum, J. G., & Wootten, A. 1993, ApJS, 89, 123
Megeath, S. T., Herter, T., Beichman, C., et al. 1996, A&A, 307, 775
Megeath, S. T., Townsley, L. K., Oey, M. S., & Tieftrunk, A. R. 2008, in Low- and High-mass Star Formation in the W3, W4, and W5 Regions, ed. B. Reipurth, 264
Megeath, S. T., Wilson, T. L., & Corbin, M. R. 2005, ApJ, 622, L141
Minier, V., Burton, M. G., Hill, T., et al. 2005, A&A, 429, 945
Mitchell, G. F., Hasegawa, T. I., & Schella, J. 1992, ApJ, 386, 604
Mitchell, G. F., Maillard, J.-P., & Hasegawa, T. I. 1991, ApJ, 371, 342
Moore, T. J. T., Bretherton, D. E., Fujiyoshi, T., et al. 2007, MNRAS, 379, 663
Mottram, J. C., Hoare, M. G., Davies, B., et al. 2011, ApJ, 730, L33
Mühle, S., Seaquist, E. R., & Henkel, C. 2007, ApJ, 671, 1579
Nomura, H., & Millar, T. J. 2004, A&A, 414, 409
Ojha, D. K., Tamura, M., Nakajima, Y., et al. 2004, ApJ, 608, 797
Ossenkopf, V., & Henning, T. 1994, A&A, 291, 943
Pillai, T., Wyrowski, F., Carey, S. J., & Menten, K. M. 2006, A&A, 450, 569
Ridge, N. A., & Moore, T. J. T. 2001, A&A, 378, 495
Rodón, J. A., Beuther, H., Megeath, S. T., & van der Tak, F. F. S. 2008, A&A, 490, 213
Ruch, G. T., Jones, T. J., Woodward, C. E., et al. 2007, ApJ, 654, 338
Sandell, G. 2000, A&A, 358, 242
Sarma, A. P., Troland, T. H., Crutcher, R. M., & Roberts, D. A. 2002, ApJ, 580, 928
Sarma, A. P., Troland, T. H., & Romney, J. D. 2001, ApJ, 554, L217

Sault, R. J., Teuben, P. J., & Wright, M. C. H. 1995, in ASP Conf. Ser. 77, Astronomical Data Analysis Software and Systems IV, ed. R. A. Shaw, H. E. Payne, & J. J. E. Hayes (San Francisco, CA: ASP), 433
Schilke, P., Benford, D. J., Hunter, T. R., Lis, D. C., & Phillips, T. G. 2001, ApJS, 132, 281
Schilke, P., Groesbeck, T. D., Blake, G. A., & Phillips, T. G. 1997a, ApJS, 108, 301
Schilke, P., Walmsley, C. M., Pineau des Forets, G., & Flower, D. R. 1997b, A&A, 321, 293
Scoville, N. Z., Carlstrom, J. E., Chandler, C. J., et al. 1993, PASP, 105, 1482
Sobolev, A. M., Cragg, D. M., Ellingsen, S. P., et al. 2007, in IAU Symp. 242, Astrophysical Masers and Their Environments, ed. J. M. Chapman & W. A. Baan (Cambridge: Cambridge Univ. Press), 81
Sutton, E. C., Blake, G. A., Masson, C. R., & Phillips, T. G. 1985, ApJS, 58, 341
Tieftrunk, A. R., Gaume, R. A., Claussen, M. J., Wilson, T. L., & Johnston, K. J. 1997, A&A, 318, 931
Tieftrunk, A. R., Gaume, R. A., & Wilson, T. L. 1998, A&A, 340, 232
van der Tak, F. F. S., Tuthill, P. G., & Danchi, W. C. 2005, A&A, 431, 993
Vasyunina, T., Linz, H., Henning, T., et al. 2011, A&A, 527, A88
Viti, S., Collings, M. P., Dever, J. W., McCoustra, M. R. S., & Williams, D. A. 2004, MNRAS, 354, 1141
Wang, Y., Beuther, H., Bik, A., et al. 2011, A&A, 527, A32
Watanabe, T., & Mitchell, G. F. 2008, AJ, 136, 1947
Wilner, D. J., Wright, M. C. H., & Plambeck, R. L. 1994, ApJ, 422, 642
Wilson, T. L., Boboltz, D. A., Gaume, R. A., & Megeath, S. T. 2003, ApJ, 597, 434
Wood, D. O. S., & Churchwell, E. 1989, ApJ, 340, 265
Wright, M. C. H., Plambeck, R. L., & Wilner, D. J. 1996, ApJ, 469, 216
Wu, Y., Wei, Y., Zhao, M., et al. 2004, A&A, 426, 503
Wynn-Williams, C. G., Becklin, E. E., & Neugebauer, G. 1972, MNRAS, 160, 1
Xu, Y., Reid, M. J., Zheng, X. W., & Menten, K. M. 2006, Science, 311, 54
Zhang, Q., Ho, P. T. P., & Ohashi, N. 1998a, ApJ, 494, 636
Zhang, Q., Hunter, T. R., Beuther, H., et al. 2007, ApJ, 658, 1152
Zhang, Q., Hunter, T. R., Brand, J., et al. 2005, ApJ, 625, 864
Zhang, Q., Hunter, T. R., & Sridharan, T. K. 1998b, ApJ, 505, L151
Zinnecker, H., & Yorke, H. W. 2007, ARA&A, 45, 481